Can mesoscale eddy kinetic energy sources and sinks be inferred from sea surface height in the Agulhas Current ?

P. Tedesco[1,2], J. Gula[1,3], P. Penven[1], C. Ménesguen[1], Q. Jamet[4], C. Vic[1]

[1]Univ. Brest, CNRS, IRD, Ifremer, Laboratoire d'Océanographie Physique et Spatiale (LOPS), IUEM, 29280, Brest, France.
[2]Imperial College of London, UK.
[3]Institut Universitaire de France (IUF), France.
[4]Institut des Géosciences de l'Environnement (IGE), France.

Key Points:

- The mesoscale EKE-fluxes divergence is mainly positive in the Agulhas Current region, denoting a net mesoscale EKE source
- The EKE-fluxes divergence mainly accounts for the advection of EKE by geostrophic flows, and more weakly for ageostrophic EKE-fluxes
- The main contribution to EKE-fluxes divergence (advection of EKE) can be qualitatively inferred in the Agulhas Current region using sea surface height

Corresponding author: Pauline Tedesco, `p.tedesco@imperial.ac.uk`

Abstract

Western boundaries (WB) have been suggested to be hotspots of mesoscale eddy decay, using an eddy kinetic energy (EKE)-fluxes divergence based on sea surface height (η). The η-based diagnostic requires approximations, including the use of geostrophic velocities. Here, we assess to what extent mesoscale EKE-fluxes divergence can be inferred from η using a numerical simulation of the Agulhas Current. Both components of the EKE-fluxes divergence are mainly positive in the WB region (net EKE sources), which is not reliably accounted by both η-based diagnostics. The η-based eddy-pressure work (linear component) gives a different result than the true one, with a net contribution of the opposite sign in the WB region. Although mesoscale eddies are mainly geostrophic, ageostrophic eddy-pressure work dominates. It can be explained by mesoscale eddies's scale to fall below the scale of $\frac{Ro|f|}{\beta}$ in the WB region. The advection of EKE (non-linear component) mainly accounts for geostrophic EKE-fluxes in the WB region It dominates the EKE-fluxes divergence in the WB region, which can therefore be qualitatively inferred using η (up to 54% of the net EKE source). Our results in the Agulhas Current show a mesoscale eddy dynamics in contrast with the decay's paradigm at western boundaries. Further analysis in other western boundaries are required to complete our understanding of mesoscale eddies dynamics.

Plain Language Summary

[Mesoscale eddies are a key component of the ocean energy budget. Although their generation are largely documented, how their energy is dissipated remains uncertain. A closure to their lifecycle — decay at western boundaries — has been suggested using an eddy kinetic energy (EKE)-fluxes divergence based on sea surface height (η). The η-based diagnostic requires several approximations, including geostrophic velocities. Understanding to what extent, mesoscale EKE-fluxes divergence can be inferred from η is a fundamental issue for ocean dynamics and study strategy. Here, we investigate the impacts of the approximations on the EKE-fluxes divergence using a numerical simulation of the Agulhas Current. We show that both components of EKE-fluxes divergence are mainly positive, denoting a net mesoscale EKE source, which is not reliably accounted by both η-based components. Advection of EKE (nonlinear component) and eddy-pressure work (linear component) mainly account for geostrophic fluxes and ageostrophic fluxes, respectively. However, the EKE-fluxes divergence is dominated by the advection of EKE, enabling its qualitative estimation using η. Our results in the Agulhas Current are favorable to η-based mesoscale EKE-fluxes divergence, but show a dynamics in contrast with the decay's paradigm at western boundaries.]

1 Introduction

Mesoscale eddies represent 90 % of the surface kinetic energy (Wunsch, 2007) and are a key component of the global ocean energy budget (Ferrari & Wunsch, 2009; Müller et al., 2005). They have horizontal scales of the order of the 1^{st} Rossby deformation radius or larger (O(30-100) km; Chelton et al. (2011)). Based on the quasi-geostrophic theory, the velocity field at these scales can be decomposed into a leading-order geostrophic and a weaker ageostrophic component (Gill, 1982). Geostrophy represents the balance of flows dominated by rotation compared to advection (Rossby number : $Ro \ll 1$) and stratification compared to vertical shear (Richardson number : $Ri \gg 1$). Ageostrophic effects ($Ro, Ri \sim O(1)$), such as advection, vertical shear and topographic interactions among others, become important at scales smaller than Rd and accounts for variations of the geostrophically-balanced system.

The characteristics of mesoscale eddies make them easily trackable by satellite altimetry, which measures sea surface height (η) – an indirect measure of geostrophic motions at the surface. Satellite altimetry allowed to improve our understanding of the ocean dynamics

by evidencing the prevalence of mesoscale eddy at the surface (Ducet et al., 2000). Although mesoscale eddies are ubiquitous across the ocean, they are the most energetic in western boundary currents and in the Antarctic Circumpolar Current (Ducet et al., 2000; Chelton et al., 2007, 2011), making these regions key spots for the global ocean energy budget.
Western boundaries have been suggested to be ubiquitous mesoscale eddy kinetic energy (EKE) sinks (Zhai et al., 2010). This suggestion closes the following paradigm of mesoscale eddy lifecycle: mesoscale eddies originate nearly everywhere in the ocean, propagate westward at about the speed of long baroclinic Rossby waves and decay upon western boundaries, likely due to direct energy routes, down to dissipation, channeled by topography (Gill et al., 1974; Zhai et al., 2010; Chelton et al., 2011; Evans et al., 2020; Z. Yang et al., 2021; Evans et al., 2022).
This scenario has been confirmed, using *in situ* measurements and idealized numerical simulations, in regions where no western boundary current was present (Evans et al., 2020; Z. Yang et al., 2021; Evans et al., 2022). However, in the presence of western boundary currents, studies based on numerical simulations show more complex mesoscale eddy dynamics. Western boundaries are hotspots of mesoscale eddy generation due to instabilities of the western boundary currents (Halo et al., 2014; Kang & Curchitser, 2015; Gula et al., 2015; Y. Yang & Liang, 2016; Yan et al., 2019; Li et al., n.d.; Jamet et al., 2021; Tedesco et al., 2022), such that local generation of mesoscale eddies may overcome the local decay of remotely-generated mesoscale eddies.

The estimation of the mesoscale EKE sink by Zhai et al. (2010) is based on an η-based diagnostic of the EKE-fluxes divergence.
The EKE-fluxes divergence has two components: the rate of the spatial redistribution of EKE done by pressure fluctuations (eddy-pressure work, usually interpreted as the linear contribution from the waves) and the nonlinear advection of EKE by the flow (Harrison & Robinson, 1978). A negative (positive) EKE-fluxes divergence indicates that incoming EKE-fluxes are larger (lower) than the outgoing ones, showing that the region is a net EKE sink (source).
The use of η to derive a vertically-integrated EKE-fluxes divergence requires three approximations for the mesoscale eddies dynamics (Zhai et al., 2010):

(i) **Mesoscale eddies are assumed to be geostrophic**. Geostrophy should be a good approximation for mesoscale eddy velocities, as assumed by the quasi-geostrophic turbulence theory (Charney, 1971) and indicated by the Rossby number of mesoscale eddies ($Ro = O(\ll 0.05)$) inferred from satellite altimetry (Chelton et al., 2011).

(ii) **The mesoscale eddy vertical structure is approximated by the 1^{st} baroclinic mode**. Mesoscale eddies have surface-intensified vertical structures energized to the bottom, represented by the combination of the barotropic and 1^{st} baroclinic vertical modes (Wunsch, 1997; Smith & Vallis, 2001; Venaille et al., 2011; Tedesco et al., 2022). η is a measure of the ocean surface dynamics and is usually interpreted as primarily reflecting the 1^{st} baroclinic mode, which has a surface-intensified structure (Wunsch, 1997; Smith & Vallis, 2001).

(iii) **Mesoscale eddies interactions with topography are neglected**. This might be justified by assuming that mesoscale EKE-fluxes have spatial variations larger than that of topography (Zhai et al., 2010).

Several studies, based on numerical simulations and using no approximations, denote a EKE-fluxes divergence in contrast with the η-based one (Harrison & Robinson, 1978; Chen et al., 2014; Capó et al., 2019). The eddy-pressure work is mainly negative and of leading-order in most regions (western boundary currents, Antarctic Circumpolar Current, Subtropical gyre and Interior Ocean). The advection of EKE is positive in most western boundary currents and in the Western Mediterranean Sea, but it is the leading-order contribution only in the latter region. It indicates that the eddy-pressure work and advection of EKE have contrasted contributions, resulting in an EKE-fluxes divergence varying between western boundaries. A recent study has shown that both mesoscale eddy-pressure work and advection of EKE are positive in the Agulhas Current region (Tedesco et al., 2022). This region is a net mesoscale EKE source, in contrast with the paradigm of ubiquitous net mesoscale EKE sinks at western boundaries.

The differences between the non-approximated and the η-based EKE-fluxes divergence question the approximations used to derive the η-based diagnostic.
Due to the leading-order geostrophic component of mesoscale eddy, satellite altimetry is a reference database for evaluating the surface mesoscale EKE reservoir. However, the question of using altimetry data to assess the sources and sinks of the mesoscale EKE reservoir remains a separate issue. The quasi-geostrophic theory states that ageostrophic motions significantly contribute to the processes sustaining the mesoscale EKE reservoir (Müller et al., 2005; Ferrari & Wunsch, 2009). While the significance of ageostrophic motions to energy transfers across scales, and especially from mesoscale eddies toward smaller scales, is asserted, its contributions to the EKE-fluxes divergence remains an open question to our knowledge.
Due to the 1^{st} baroclinic mode being surface-intensified, surface geostrophic velocities derived from satellite altimetry data are usually interpreted as primarily reflecting this vertical mode (Wunsch, 2007; Smith & Vallis, 2001). However, this questions the interpretation of the η-based EKE-fluxes divergence as the one of the mesoscale reservoir, which is formally represented by the barotropic and 1^{st} baroclinic modes (Wunsch, 1997; Smith & Vallis, 2001; Venaille et al., 2011). This question is supported by the mesoscale EKE reservoir being equipartitioned between both modes, or even locally dominated by the barotropic mode, in the western boundary region of the Agulhas Current (Tedesco et al., 2022).
Topographic interactions are documented to be key processes of mesoscale eddy dynamics at western boundaries. Topography controls the triggering of mesoscale eddy generation by instability processes (Lutjeharms, 2006; Gula et al., 2015) and channels energy transfers between mesoscale eddies, eddies of smaller scale, waves and mean currents (Adcock & Marshall, 2000; Nikurashin & Ferrari, 2010; Evans et al., 2020; Perfect et al., 2020; Tedesco et al., 2022). The contribution of topographic interactions to mesoscale EKE-fluxes divergence remain to be determined.

The use of altimetry data to infer the mesoscale EKE-fluxes divergence depends on the impact of the three aforementioned approximations – (i) geostrophy *vs.* ageostrophy, (ii) 1^{st} baroclinic *vs.* barotropic modes and (iii) importance of topographic interactions – in regions of western boundary. Knowing to what extent altimetry data allows to infer the EKE-fluxes divergence is a fundamental issue for reliable study strategy of mesoscale EKE dynamics and, subsequently, for understanding the global ocean dynamics.
We aim to assess the mesoscale EKE-fluxes divergence in a western boundary current, using a regional numerical simulation, and to characterize if approximations (i), (ii), and (iii) allow to characterize its main contributions. We focus on the Agulhas Current, which is the western boundary current of the South Indian Ocean Subtropical gyre (Lutjeharms, 2006). It represents a sub-region of the South Western Indian Ocean, which has been suggested as the largest mesoscale EKE sink by Zhai et al. (2010).

Our study is organized around the following questions : Do the η-based components of the EKE-fluxes divergence (eddy-pressure work and advection of EKE) provide reliable estimates of the true ones ? If not, which approximations are responsible for differences ? What does it imply for inferring the EKE-fluxes divergence using η field ?
The true and η-based expressions of EKE-fluxes divergence components (eddy-pressure work and advection of EKE) are defined and interpreted in section 2. The η-based paradigm

of mesoscale EKE sink at western boundaries (Zhai et al., 2010) is evaluated using observations and a numerical simulation in section 3. The validity of the η-based components are evaluated and the main contributions of the true components are characterized, respectively in section 4 and 5. The results of sections 4 and 5 are sum up in section 6 to draw a conclusion on the use of satellite altimetry data to infer the EKE-fluxes divergence. The results are then discussed in a larger context of observation-based EKE budgets and of mesoscale eddy dynamics in section 7.

2 Theory

We present in the following the modal EKE-fluxes divergence. We first present the theoretical framework of vertical modes. We then define the true expression of the EKE-fluxes divergence, constituted of the modal eddy-pressure work (**EPW**) and the advection of EKE (**AEKE**), based on Tedesco et al. (2022). We finally detail the approximations that are required to derive their η-based expressions.

2.1 Vertical modes

A convenient approach to describe the vertical structure of mesoscale motions is the modal decomposition using traditional vertical modes (Gill, 1982). The vertical structure of the mesoscale EKE reservoir corresponds to the combination of the barotropic and 1^{st} baroclinic modes (Wunsch, 1997; Smith & Vallis, 2001; Venaille et al., 2011; Tedesco et al., 2022), which represents surface-intensified vertical structures energized to the bottom.

The vertical modes ϕ_n for the horizontal velocity ($\mathbf{u}$) and the dynamical pressure (p) are the eigenfunctions solution of the Sturm-Liouville problem (Eq. 1), using linearized free-surface ($|\frac{\partial}{\partial z}\phi_n|_{z=\eta} = |\frac{-N^2}{g}\phi_n|_{z=\eta}$) and flat-bottom boundary conditions ($|\frac{\partial}{\partial z}\phi_n|_{z=-H} = 0$) :

$$\frac{\partial}{\partial z}\left(\frac{1}{N^2}\frac{\partial}{\partial z}\phi_n\right) + \frac{1}{c_n^2}\phi_n = 0 \tag{1}$$

with N^2 the time-averaged buoyancy frequency, g the acceleration of gravity and $c_n^2 = \frac{1}{n\pi}\int_{-H}^{\eta} N(\mathbf{x}, z)\; dz$ the eigenvalues of the vertical modes.
The vertical modes are related to horizontal scales via c_n^2, which are good approximations of the Rossby baroclinic deformation radii : $Rd_{n\geq 1} = \frac{c_n}{|f|} \approx \frac{1}{n\pi|f|}\int_{-H}^{\eta} N(\mathbf{x}, z)\; dz$ (Chelton et al., 1998), with f the Coriolis parameter.
The modal base ϕ_n satisfies the orthogonality condition :

$$\int_{-H}^{\eta} \phi_m\phi_n\; dz = \delta_{mn}h \tag{2}$$

with δ_{mn} the usual Kronecker symbol and $h = \eta + H$ the water column depth.
The dynamical variables are projected onto n vertical modes as follows :

$$[\mathbf{u}_n(\mathbf{x}, t), \frac{1}{\rho_0}p_n(\mathbf{x}, t)] = \frac{1}{h}\int_{-H}^{\eta}[\mathbf{u}(\mathbf{x}, z, t), \frac{1}{\rho_0}p(\mathbf{x}, z, t)]\phi_n(\mathbf{x}, z)\; dz \tag{3}$$

with $\mathbf{u}_n$ and p_n the modal amplitudes of the horizontal velocity ($\mathbf{u}$) and dynamical pressure (p) and ρ_0 the reference density value.

2.2 True expression of the modal EKE-fluxes divergence

The modal EKE-fluxes divergence is a contribution of the modal EKE budget. The modal EKE budget corresponds to the classic EKE budget (Harrison & Robinson, 1978; Gula et al., 2016) derived in the framework of the vertical modes. Tedesco et al. (2022)

derived a comprehensive modal EKE budget in the context of the mesoscale variability, inspired from the budget derived in the context of internal tides (Kelly, 2016). The modal EKE budget reads as follows :

$$\underbrace{\mathbf{u_n'} \cdot (h\frac{\partial}{\partial_t}\mathbf{u_n'})}_{Time\ rate} + \underbrace{\underbrace{\nabla_H \cdot \int_{-H}^{\eta} \mathbf{u'}_n p_n' \phi_n^2 \ dz}_{Eddy-pressure\ work\ (\mathbf{EPW})} + \underbrace{\frac{\rho_0}{2}\nabla_H \cdot \int_{-H}^{\eta} \mathbf{u}_n \phi_n ||\mathbf{u}_n' \phi_n||^2 \ dz}_{Advection\ of\ EKE\ (\mathbf{AEKE})}}_{Modal\ EKE-fluxes\ divergence\ (\mathbf{EPW+AEKE})}$$
$$= \sum \left(\underbrace{S_n}_{EKE\ sources} + \underbrace{D_n}_{EKE\ sinks} \right) \tag{4}$$

with the prime denoting fluctuations relative to the 1995-2004 time average. Terms are averaged over this period. The dynamical pressure ($p(\mathbf{x}, z, t)$) is derived from the *in situ* density ($\rho(\mathbf{x}, z, t)$) from which the background density profile ($\widetilde{\rho}(z)$ defined as the spatial and time average of the *in situ* density) as been substracted.

The modal EKE-fluxes divergence corresponds to the rate of the spatial redistribution of modal EKE done by pressure fluctuations (**EPW**) and by advection (**AEKE**). The **EPW** is usually interpreted as the linear wave contribution, and **AEKE** as the advection of $\overline{EKE}$ by the total flow (Harrison & Robinson, 1978).
In the context of linear theories of internal waves (Kelly et al., 2010, 2012; Kelly, 2016) and of Rossby waves (Masuda, 1978), **EPW** is the only contribution to the modal EKE-fluxes divergence. For interior-ocean dynamics it represents the main contribution (Harrison & Robinson, 1978). In regions of high variability, **AEKE** can significantly contribute to the EKE-fluxes divergence and can be equivalent to **EPW** (Harrison & Robinson, 1978; Capó et al., 2019; Tedesco et al., 2022).

The mesoscale eddy dynamics modeled by our numerical simulation is in equilibrium for the period considered in our study (1995-2004). The time rate smallness has indeed been evaluated by Tedesco et al. (2022) for the period 1995-1999, which is shorter than the period 1995-2004 used here. The EKE-fluxes divergence therefore accounts for the left hand side of the EKE budget (Eq. 4). It equals the sum of all local EKE sources (S_n) and sinks (D_n). It can therefore be interpreted as the redistribution rate of the net EKE sources and sinks. A negative (positive) EKE-fluxes divergence indicates that the ingoing EKE-fluxes are larger (lower) than the outgoing ones, resulting in a net EKE sink (source), whose content has been imported (exported).

In the present study, we focus on the EKE-fluxes divergence of the mesoscale reservoir, that we define as the sum of the barotropic ($n = 0$) and 1^{st} baroclinic ($n = 1$) components ($\mathbf{EPW_{n=0-1}}$ and $\mathbf{AEKE_{n=0-1}}$ that are referred in the following as **EPW** and **AEKE** for purpose of simplify notation).

2.3 η-based expressions of the modal EKE-fluxes divergence

We define here alternative expressions based on η for the components of the EKE-fluxes divergence. We define the different η-based expressions of **EPW**, gradually accounting for approximations (i), (ii) and (iii) used in (Zhai et al., 2010). We also define an η-based expression of **AEKE** accounting for approximation (i). The main terms discussed in this study are listed in Table 1.

2.3.1 Approximation (i) ($\mathbf{EPW_{(i)}}$ *and* $\mathbf{AEKE_{(i)}}$ *)*

EPW and **AEKE** (Eq. 4) can be written as the sum of three contributions, as follows :

$$\mathbf{EPW} = \underbrace{\int_{-H}^{\eta} p'_n\phi_n \nabla_H \cdot (\mathbf{u}'_n\phi_n)\ dz}_{\mathbf{A}} + \underbrace{\int_{-H}^{\eta} (\mathbf{u}'_n\phi_n)\cdot\nabla_H(p'_n\phi_n)\ dz}_{\mathbf{B}} \tag{5}$$
$$+ \underbrace{\nabla_H\eta \cdot |\mathbf{u}'_n p'_n\phi_n^2|_{z=\eta} + \nabla_H H \cdot |\mathbf{u}'_n p'_n\phi_n^2|_{z=-H}}_{\mathbf{C}}$$

$$\mathbf{AEKE} = \underbrace{\frac{\rho_0}{2}\int_{-H}^{\eta} ||\mathbf{u}'_n\phi_n||^2 \nabla_H\cdot(\mathbf{u}_n\phi_n)\ dz}_{\mathbf{A}} + \underbrace{\frac{\rho_0}{2}\int_{-H}^{\eta}(\mathbf{u}_n\phi_n)\cdot\nabla_H||\mathbf{u}'_n\phi_n||^2\ dz}_{\mathbf{B}} \tag{6}$$
$$+ \underbrace{\frac{\rho_0}{2}\nabla_H\overline{\eta}\cdot\overline{|\mathbf{u}_n\phi_n||\mathbf{u}'_n\phi_n||^2}|_{z=\eta} + \frac{\rho_0}{2}\nabla_H H\cdot|\mathbf{u}_n\phi_n||\mathbf{u}'_n\phi_n||^2|_{z=-H}}_{\mathbf{C}}$$

Terms **C** represent the interactions of EKE-fluxes with topography ($-H$) and sea surface height (η) gradients. It can be further simplified as : $\nabla_H H \cdot |\overline{\mathbf{u}'_n p'_n}\phi_n^2|_{z=-H}$, because : $||\nabla_H\overline{\eta}|| = O(10^{-4})||\nabla_H H||$ in the Agulhas Current region.

EPW (Eq. 5) and **AEKE** (Eq. 6) can be written as $\mathbf{EPW_{(i)}}$ (Eq. 7) and $\mathbf{AEKE_{(i)}}$ (Eq. 8) when using the approximation of (i) modal geostrophic velocities ($\mathbf{u}'_{g,n}\phi_n$). The velocities are expressed using modulated η fields, which account for the fraction of the different vertical modes ($\mathbf{u}_{g,n}\phi_n = \mathbf{k}\wedge\frac{g}{f}\nabla_H\left(\frac{\phi_n}{|\phi_n|_{z=0}}\lambda_n\eta\right)$ with $\lambda_n = \frac{\eta_n}{\eta}$ and $\mathbf{u}'_{g,n}\phi_n = \mathbf{k}\wedge\frac{g}{f}\nabla_H\left(\frac{\phi_n}{|\phi_n|_{z=0}}\alpha_n\eta'\right)$ with $\alpha_n = \frac{\eta'_n}{\eta'}$).

$$\mathbf{EPW_{(i)}} = \underbrace{-\frac{\beta\rho_0 g^2}{2f^2}\frac{\partial}{\partial_x}\left(\frac{\int_{-H}^{\eta}\phi_n^2\ dz}{|\phi_n^2|_{z=0}}\alpha_n^2\eta'^2\right)}_{\beta-contribution\ (\mathbf{A1})} + \underbrace{\frac{\beta\rho_0 g^2}{2f^2}\frac{\partial H}{\partial_x}\frac{|\phi_n^2|_{z=-H}}{|\phi_n^2|_{z=0}}\alpha_n\eta'^2}_{\beta-contribution\ to\ topographic\ interactions\ (\mathbf{A2})} \tag{7}$$
$$+ \underbrace{\frac{\rho_0 g^2}{2f}\nabla_H H\cdot|\mathbf{k}\wedge\nabla_H\left(\frac{\phi_n^2}{|\phi_n^2|_{z=0}}\right)\alpha_n\eta'^2|_{z=-H}}_{EKE\ fluxes-topographic\ interactions\ (\mathbf{C})}$$

With approximation (i), the contribution of horizontal modal pressure gradients (**B** in Eq. 5) cancels out. $\mathbf{EPW_{(i)}}$ accounts then for a β-contribution (**A1**) and for the contributions of β-effect (**A2**) and EKE-fluxes to topographic interactions (**C**).

$$\mathbf{AEKE_{(i)}} = \underbrace{-\frac{\beta\rho_0 g}{2f^2}\int_{-H}^{\eta}||\mathbf{u}'_{g,n}\phi_n||^2\frac{\partial}{\partial_x}\left(\frac{\phi_n}{|\phi_n|_{z=0}}\lambda_n\eta\right)\ dz}_{\beta-contribution\ (\mathbf{A})} + \underbrace{\frac{\rho_0}{2}\int_{-H}^{\eta}(\mathbf{u}_{g,n}\phi_n)\cdot\nabla_H||\mathbf{u}'_{g,n}\phi_n||^2\ dz}_{Work\ of\ eddy-total\ flow\ interactions\ (\mathbf{B})} \tag{8}$$
$$+ \underbrace{\frac{\rho_0}{2}\nabla_H H\cdot|\mathbf{u}_{g,n}\phi_n||\mathbf{u}'_{g,n}\phi_n||^2|_{z=-H}}_{EKE\ fluxes-topographic\ interactions\ (\mathbf{C})}$$

$\mathbf{AEKE_{(i)}}$ (Eq. 8) accounts for a β-contribution (**A**), the work of eddy-total flow interactions (**B**) and for the EKE-fluxes contribution to topographic interactions (**C**).
We present in the following the use of approximations (ii) and (iii) leading to the η-based **EPW** defined by Zhai et al. (2010).

2.3.2 Approximation (ii) ($\mathbf{EPW_{(i,ii)}}$)

$\mathbf{EPW_{(i)}}$ (Eq. 7) can be written as $\mathbf{EPW_{(i,ii)}}$ (Eq. 9) when using the approximation of (ii) η primarily reflecting the 1^{st} baroclinic mode ($\alpha_n \sim \alpha_1$), such as :

$$\overline{\mathbf{EPW}}_{\mathbf{(i,ii)}} = \underbrace{-\frac{\beta\rho_0 g^2}{2f^2}\frac{\partial}{\partial_x}\left(\frac{\int_{-H}^{\overline{\eta}}\phi_1^2\,dz}{|\phi_1^2|_{z=0}}\overline{\eta'^2}\right)}_{\beta-contribution\ (\mathbf{A1})} + \underbrace{\frac{\beta\rho_0 g^2}{2f^2}\frac{\partial H}{\partial_x}\frac{|\phi_1^2|_{z=-H}}{|\phi_1^2|_{z=0}}\overline{\eta'^2}}_{\beta-contribution\ to\ topographic\ interactions\ (\mathbf{A2})}$$
$$+ \underbrace{\frac{\rho_0 g^2}{2f}\nabla_H H\cdot|\mathbf{k}\wedge\nabla_H\left(\frac{\phi_1^2}{|\phi_1^2|_{z=0}}\right)\overline{\eta'^2}|_{z=-H}}_{EKE\ fluxes-topographic\ interactions\ (\mathbf{C})} \tag{9}$$

2.3.3 Approximation (iii) ($\mathbf{EPW_{(i,ii,iii)}}$ and $\mathbf{EPW_{(i,iii)}}$)

$\mathbf{EPW_{(i,ii)}}$ (Eq. 9) can be written as $\mathbf{EPW_{(i,ii,iii)}}$ (Eq. 10) when using the approximation of (iii) topographic interactions (**A2**, **C**) being negligible compared to the β-contribution (**A1**), such that :

$$\mathbf{EPW_{(i,ii,iii)}} = \underbrace{-\frac{\beta\rho_0 g^2}{2f^2}\frac{\partial}{\partial_x}\left(\frac{\int_{-H}^{\eta}\phi_1^2\,dz}{|\phi_1^2|_{z=0}}\eta'^2\right)}_{\beta-contribution\ (\mathbf{A1})} \tag{10}$$

The expression of $\mathbf{EPW_{(i,ii,iii)}}$ (Eq. 10) points toward the contribution of the linear EKE-fluxes, driven by the β-effect, acting on the 1^{st} baroclinic mode (Zhai et al., 2010). We additionally define $\mathbf{EPW_{(i,iii)}}$ (Eq. 11), which is an equivalent expression to that of $\mathbf{EPW_{(i,ii,iii)}}$ (Eq. 10) at the difference that approximation (ii) is relaxed, such that :

$$\mathbf{EPW_{(i,iii)}} = \underbrace{-\frac{\beta\rho_0 g^2}{2f^2}\frac{\partial}{\partial_x}\left(\frac{\int_{-H}^{\eta}\phi_n^2\,dz}{|\phi_n^2|_{z=0}}\alpha_n^2\eta'^2\right)}_{\beta-contribution\ (\mathbf{A1})} \tag{11}$$

The aim of this study is to assess if the approximated $\mathbf{EPW_{(i,ii,iii)}}$ (Eq. 10) and $\mathbf{AEKE_{(i)}}$ (Eq. 8) account for the main contributions to the true **EPW** (Eq. 4) and **AEKE** (Eq. 4). To do so, we assess the impacts of approximations (i), (ii) and (iii) on $\mathbf{EPW_{(i,ii,iii)}}$ in section 4 and the impact of approximations (i) on $\mathbf{AEKE_{(i)}}$ in section 5. The main terms discussed in these sections are summarized in Table 1.

Acronym	Expression	Description
EPW (Eq. 5)	$\nabla_H \cdot \int_{-H}^{\eta} \mathbf{u'}_n p'_n \phi_n^2 \; dz$	true mesoscale eddy-pressure work
$\mathbf{EPW_{(i)}}$ (Eq. 7)	$-\frac{\beta\rho_0 g^2}{2f^2}\frac{\partial}{\partial_x}\left(\frac{\int_{-H}^{\eta}\phi_n^2 \; dz}{\|\phi_n^2\|_{z=0}}\alpha_n\eta'^2\right)$ $+\frac{\beta\rho_0 g^2}{2f^2}\frac{\partial H}{\partial x}\frac{\|\phi_n^2\|_{z=-H}}{\|\phi_n^2\|_{z=0}}\alpha_n\eta'^2$ $+\frac{\rho_0 g^2}{2f}\nabla_H H\cdot\|\mathbf{k}\wedge\nabla_H\left(\frac{\phi_n^2}{\|\phi_n^2\|_{z=0}}\right)\alpha_n\eta'^2\|_{z=-H}$, with $\alpha_n=\frac{\eta_n'^2}{\eta'^2}$	η-based mesoscale eddy-pressure work using approximation (i)
$\mathbf{EPW_{(i,ii,iii)}}$ (Eq. 10)	$-\frac{\beta\rho_0 g^2}{2f^2}\frac{\partial}{\partial_x}\left(\frac{\int_{-H}^{\eta}\phi_1^2 \; dz}{\|\phi_1^2\|_{z=0}}\eta'^2\right)$	η-based mesoscale eddy-pressure work using approximations (i), (ii) and (iii)
$\mathbf{EPW_{(i,iii)}}$ (Eq. 11)	$\frac{\beta\rho_0 g^2}{2f^2}\frac{\partial}{\partial_x}\left(\frac{\int_{-H}^{\eta}\phi_n^2 \; dz}{\|\phi_n^2\|_{z=0}}\alpha_n\eta'^2\right)$, with $\alpha_n=\frac{\eta_n'^2}{\eta'^2}$	η-based mesoscale eddy-pressure work using approximation (i) and (iii)
AEKE (Eq. 6)	$\frac{\rho_0}{2}\nabla_H \cdot \int_{-H}^{\eta} \mathbf{u}_n\phi_n\|\|\mathbf{u}'_n\phi_n\|\|^2 \; dz$	true advection of mesoscale EKE by the total flow
$\mathbf{AEKE_{(i)}}$ (Eq. 8)	$-\frac{\beta\rho_0 g}{2f^2}\int_{-H}^{\eta}\|\|\mathbf{u}'_{g,n}\phi_n\|\|^2\partial_x(\frac{\phi_n}{\|\phi_n\|_{z=0}}\lambda_n\eta) \; dz$ $+\frac{\rho_0}{2}\int_{-H}^{\eta}(\mathbf{u}_{g,n}\phi_n)\cdot\nabla_H\|\|\mathbf{u}'_{g,n}\phi_n\|\|^2 \; dz$ $+\frac{\rho_0}{2}\nabla_H H\cdot\|\mathbf{u}_{g,n}\phi_n\|\|\mathbf{u}'_{g,n}\phi_n\|\|^2\|_{z=-H}$, with $\lambda_n=\frac{\eta_n}{\eta}$	η-based advection of mesoscale EKE by the total flow using approximation (i)

Table 1: Summary of the true and η-based expressions of the eddy-pressure work (**EPW**) and advection of mesoscale EKE by the total flow (**AEKE**) constituting the mesoscale EKE ($EKE_{n=0-1}$)-fluxes divergence.

3 Method

3.1 Observations and numerical model

We first present the observations and the regional numerical simulation used in this study. We then assess the sensitivity of the paradigm of mesoscale eddy decay at the Agulhas Current region, by comparing the observed and modeled $\mathbf{EPW_{(i,ii,iii)}}$ (Eq. 10). The term requires vertical modes (derived using a time-averaged stratification N^2) and η fields.

3.1.1 Observations

The WOCE (World Ocean Circulation Experiment) and WOA18 (World Ocean Atlas) climatologies provide *in situ* temperature and salinity fields at a global scale, with respective horizontal resolutions of 1/2° and 1°, for monthly compositing means (Gouretski & Koltermann, 2004; Locarnini et al., 2018; Zweng et al., 2019). Vertical modes are derived from the time-averaged stratification, computed from temperature and salinity provided by both climatologies. Altimetric data are mapped on a regular 1/4°- and 1/3°-grid by AVISO (Archiving, Validation and Interpretation of Satellite Oceanographic data) and provide η field for weekly compositing means at a global scale.

Here we focus on a subset of data over the Agulhas Current region (15°E - 34°E and 27°S - 40°S) for the 1995-2004 period. .

3.1.2 Numerical model

A regional numerical simulation of the Agulhas Current was performed using the Coastal and Regional COmmunity (CROCO) model. It is a free surface model, based on ROMS (Shchepetkin & McWilliams, 2005), which solves the primitive equations in the Boussinesq and hydrostatic approximations using a terrain following coordinate system (Debreu et al., 2012).
The simulation has a horizontal resolution of dx $\sim$ 2.5 km and 60 vertical levels. It encompasses the Agulhas Current region from its source, north of the Natal Bight (27°S), to the Agulhas Retroflection ($\sim$ 37°S), from where it becomes the Agulhas Return Current and flows eastward. Boundary conditions are supplied by two lower-resolution grids (dx $\sim$ 22.5 km and 7.5 km, respectively covering most of the South Indian Ocean and its western part). The surface forcing is provided by a bulk-formulation using daily relative winds. The regional numerical simulation settings and modeled mesoscale eddy dynamics are presented in details by Tedesco et al. (2019, 2022).

Vertical modes are derived from the time-averaged stratification over the 1995-2004 period, computed from the modeled temperature and salinity.

3.2 $\mathbf{EPW_{(i,ii,iii)}}$ from observations and a numerical model

In order to ensure the ability of the model to reproduce a realistic mesoscale eddy dynamics and to assess the sensitivity of the paradigm of mesoscale eddy decay at the Agulhas Current region, we compare $\mathbf{EPW_{(i,ii,iii)}}$ (Eq. 10) computed from observations (as computed in Zhai et al. (2010)) and from the model (Figure 1).

Observed and modeled $\mathbf{EPW_{(i,ii,iii)}}$ are in fairly good agreement across the domain of the dx $\sim$ 2.5 km grid (Figure 1).
Both $\mathbf{EPW_{(i,ii,iii)}}$ are most intense at the Retroflection and along the Agulhas Return Current (O(0.1-0.5) W m^{-2}) and are least intense along the Agulhas Current and in the Subgyre

(O(0.01-0.1) W m^{-2}). However, the Agulhas Current region – from north of the Natal Bight ($\sim$ 27°S) to the African tip ($\sim$ 37°S) and from the shelf to about 150 km offshore, a typical width of western boundary currents (black region in Figure 1) – stands out for both. In this region, $\mathbf{EPW}_{\mathbf{(i,ii,iii)}}$ is almost uniformly negative and has a cumulative net contribution of magnitude O(-1) GW.
The negative $\mathbf{EPW}_{\mathbf{(i,ii,iii)}}$ along the Agulhas Current – referred as the Western Boundary (WB) region in the following – is consistent with the hotspot of EKE sink in the region near the western boundary of the South Indian Ocean (poleward of $10°S$) suggested by Zhai et al. (2010).

The main discrepancy between the observed and modeled $\mathbf{EPW}_{\mathbf{(i,ii,iii)}}$ is the magnitude of the cumulative EKE sinks in the WB region. It is larger by a factor almost of 2 in the observations (Figure 1a,b). The magnitude difference is still present when using smoothed η, with a length scale of 100 km, in the model to mimic the altimetry data processing done by AVISO (Figure 1d). It indicates that the EKE sink in the WB region is robust to altimetry data processing and that horizontal scales $< O(100)$ km do not significantly contribute to the $\mathbf{EPW}_{\mathbf{(i,ii,iii)}}$ term. Using different climatologies (1/2° WOCE or 1° WOA18) and satellite altimetry data of different resolutions (1/4° or 1/3° AVISO) (Figure 1a,b) also do not significantly change the result.

The magnitude difference is unlikely explained by the forcing of remotely-eddies in the dx $\sim$ 2.5 km grid. The grid is forced at each time steps at the boundaries by a parent grid (dx $\sim$ 7.5 km), which resolves mesoscale eddies of scales $<$ 100 km.
An explanation can be the slight underestimation of the surface EKE reservoir in the dx $\sim$ 2.5 km simulation, compared to AVISO, in the Subgyre region (Figure 2 in Tedesco et al. (2022)). A weaker EKE reservoir can lead to a weaker spatial redistribution of the EKE (EKE-fluxes divergence). It is supported by the observed $\mathbf{EPW}_{\mathbf{(i,ii,iii)}}$ showing slightly larger magnitudes (-0.1 W m^{-2}) than the modeled $\mathbf{EPW}_{\mathbf{(i,ii,iii)}}$ term (-0.05 W m^{-2}), in the same areas where the surface EKE based on AVISO is slightly larger (0.05 m^2 s^{-2}) than the modeled one ($>$ 0.03 m^2 s^{-2}).
Another explanation can be the definition of the WB region. The uniform EKE sink denoted by $\mathbf{EPW}_{\mathbf{(i,ii,iii)}}$ has a larger extension in the observations than in the model (Figure 1). With a typical width of western boundary currents, the WB region fully encompasses the uniform modeled EKE sink, the southern face closely follows the $O(0)$ W m^{-1} isoline. While it encompasses most, but not all of the uniform observed EKE sink.

Both observed and modeled $\mathbf{EPW}_{\mathbf{(i,ii,iii)}}$ are mainly negative in the WB region, denoting a net EKE sink. It is consistent with the paradigm of the decay of remotely-generated mesoscale eddy at western boundaries (Zhai et al., 2010). It also confirms our choice of the dx $\sim$ 2.5 km numerical simulation to assess the η-based diagnostic of EKE-fluxes divergence in the WB region.

4 Results I : Validity of the approximated $\mathbf{EPW}_{\mathbf{(i,ii,iii)}}$ and main contributions to the true EPW

In this section we evaluate the η-based estimation of the **EPW** term ($\mathbf{EPW}_{\mathbf{(i,ii,iii)}}$). We first evaluate if $\mathbf{EPW}_{\mathbf{(i,ii,iii)}}$ (Eq. 10) is a reliable approximation of the true **EPW** (Eq. 4). We then evaluate separately the impacts of approximations (i), (ii) and (iii) (cf. section 2.1.3) and we characterize what are the main contributions to the true **EPW**.

4.1 Comparison between approximated $\mathbf{EPW_{(i,ii,iii)}}$ and true EPW

$\mathbf{EPW_{(i,ii,iii)}}$ and **EPW** in Figures 2a,b – and in all the following Figures – have been smoothed using a 75 km-radius Gaussian kernel. Smoothed terms emphasize the large-scale patterns driving the cumulative contributions of **EPW** in the WB region and ease the comparison with $\mathbf{EPW_{(i,ii,iii)}}$. The smoothing length scale corresponds to a typical mesoscale eddy radius at mid-latitudes, as inferred from satellite altimetry (Chelton et al., 2011). The sensitivity of the **EPW** term to the smoothing length scale is presented in Appendix A.

$\mathbf{EPW_{(i,ii,iii)}}$ and **EPW** strongly differ by their patterns across the whole domain and by their cumulative contributions in the WB region (Figures 2a and b). $\mathbf{EPW_{(i,ii,iii)}}$ is mainly negative in the WB region (-1.10 GW; Figure 2a) while **EPW** is mainly positive (0.81 GW; Figure 2b).

EPW denotes contrasted net mesoscale EKE sources and sinks within the WB region, consistent with the documented Agulhas Current mesoscale variability (Lutjeharms, 2006; Paldor & Lutjeharms, 2009; Tedesco et al., 2022). Along the northern and stable Agulhas Current branch (upstream of Port Elizabeth), **EPW** is negative (O(-0.01) W m^{-2}), except at the Natal Bight ($\sim$ 31°E) where Natal Pulses are generated (Elipot & Beal, 2015). Along the southern and unstable current branch (downstream of Port Elizabeth), **EPW** is positive over the entire width of the WB region, except at the Agulhas Bank tip ($\sim$ 23°E) where mesoscale EKE is locally lost.
The cumulative contribution of **EPW** across the WB region is dominated by the net mesoscale EKE sources (**EPW** > 0), which are most intense along the southern current branch where mesoscale variability is high. The locally gained mesoscale EKE is transported downstream. It mainly exits the WB region by its western face toward the South-East Atlantic Ocean or entering back the South Indian Ocean following the Agulhas Return Current (vector field in Figure 2b).

The negative $\mathbf{EPW_{(i,ii,iii)}}$ and the positive **EPW** support opposite paradigms of mesoscale eddy dynamics in the WB region. The η-based version highlights a local decay of remotely-generated mesoscale eddies, while the true version is dominated by a local generation of mesoscale eddies, which are then exported downstream. It indicates that $\mathbf{EPW_{(i,ii,iii)}}$ (Eq. 10) – β-contribution acting on the 1^{st} baroclinic mode – does not represent the main contribution to the true **EPW** (Eq. 5). This suggests that the contribution of β-effect acting on the 1^{st} baroclinic mode is counterbalanced by other dynamical processes to produce a positive **EPW** in the WB. We investigate in the following which of the approximations (i), (ii) and (iii) (cf. section 2.1.3) limits the η-based diagnostic of **EPW**.

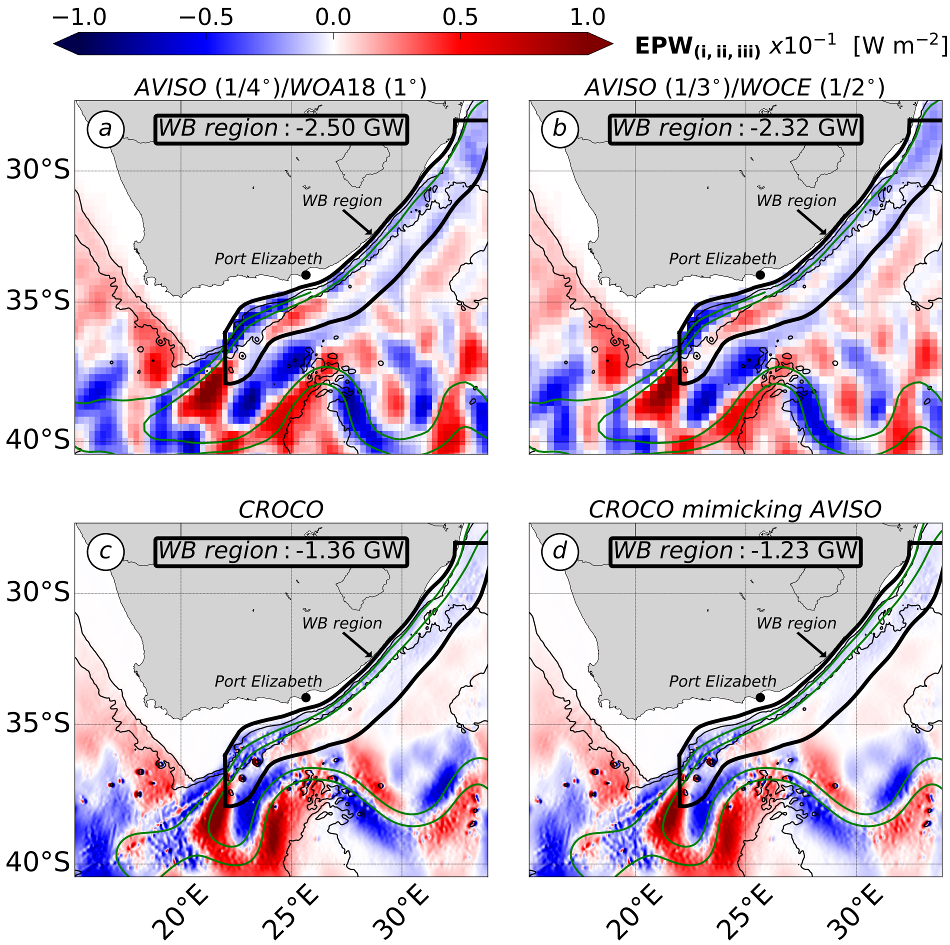

Figure 1: $\mathbf{EPW}_{(\mathbf{i},\mathbf{ii},\mathbf{iii})}$ (Eq. 10) [W m^{-2}] for (a) AVISO new products (1/4°) and WOA18 (1°) climatology, (b) AVISO old products (1/3°) and WOCE (1/2°) climatology, (c) CROCO (dx $\sim$ 2.5 km) and (d) CROCO mimicking AVISO processing (η fields smoothed with a Gaussian kernel of length scale of 100 km). Terms are averaged over the 1995-2004 period. The black area denotes the Western Boundary (WB) region and the terms integral in the region are in [GW] (10^9 W). The green contours denote the 0.25 m and 0.5 m isolines of $\overline{\eta}$ and the black contours denote the 1000 m and 3000 m isobaths. (d) Small scales patterns, visible in spite of the smoothed η fields, are due to horizontal gradients of the modeled 1^{st} baroclinic mode which is at the model resolution dx $\sim$ 2.5 km (Eq. 10). The observed and modeled $\mathbf{EPW}_{(\mathbf{i},\mathbf{ii},\mathbf{iii})}$ denote, in good agreement, an almost uniform net EKE_1 sink in the WB region ($\mathbf{EPW}_{(\mathbf{i},\mathbf{ii},\mathbf{iii})} < 0$), consistently with the paradigm of the decay of remotely-generated mesoscale eddies upon western boundaries (Zhai et al., 2010).

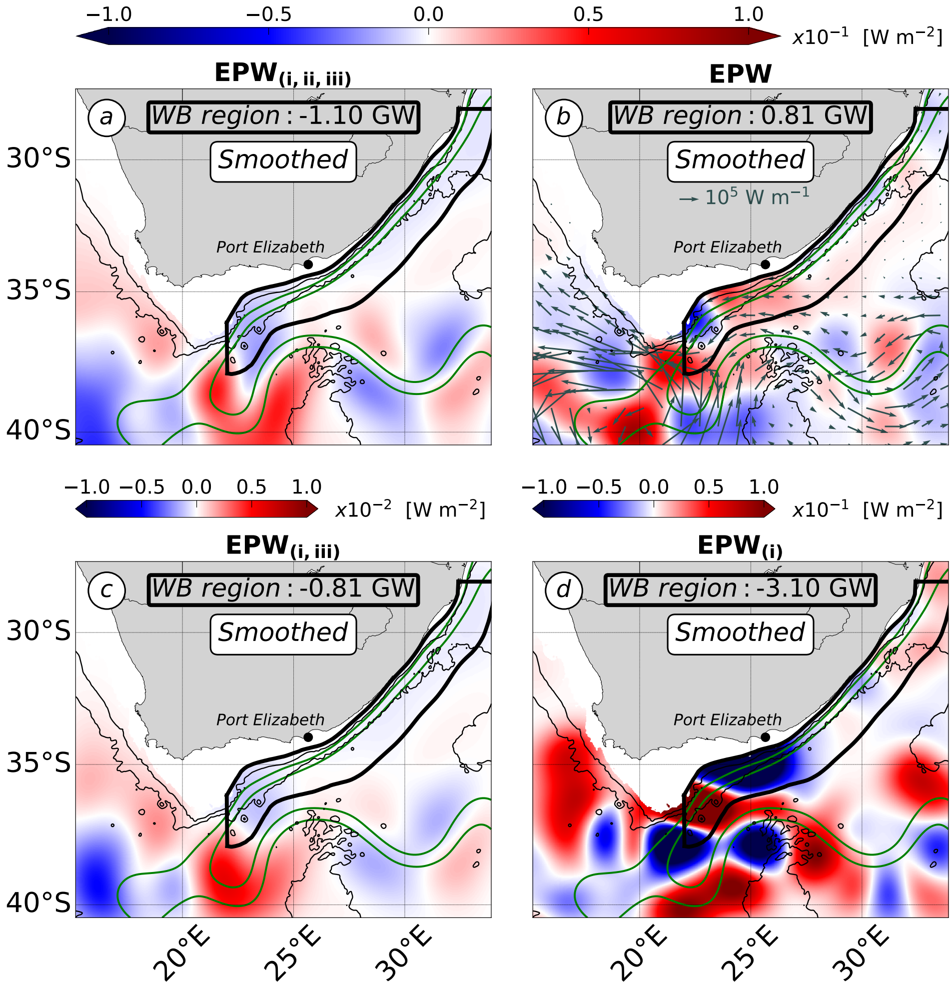

Figure 2: (a) $\mathbf{EPW}_{(\mathbf{i,ii,iii})}$ (Eq. 10), (b) $\mathbf{EPW}$ (Eq. 5 with $n = 0-1$), (c) $\mathbf{EPW}_{(\mathbf{i,iii})}$ (Eq. 11) and (d) $\mathbf{EPW}_{(\mathbf{i})}$ (Eq. 7) [W m^{-2}]. Vector field in (b) denotes the linear EKE_{0-1}-fluxes ($\int_{-H}^{\eta} \mathbf{u}'_{0-1}p'_{0-1}\phi 0 - 1^2\ dz$) [W m^{-1}]. Terms are averaged over the 1995-2004 period and smoothed with a 75 km-radius Gaussian kernel. The black area denotes the Western Boundary (WB) region and the terms integral in this region are in [GW] (10^9 W). The green contours denote the 0.25 m and 0.5 m isolines of $\overline{eta}$ and black contours denote the 1000 m and 3000 m isobaths. (a) and (b) characterize the WB region respectively as a net EKE_{0-1} sink ($\mathbf{EPW}_{(\mathbf{i,ii,iii})} < 0$) and source ($\mathbf{EPW} > 0$), supporting opposite mesoscale eddy dynamics upon the WB region. (a) $\mathbf{EPW}_{(\mathbf{i,ii,iii})}$ therefore does not account for the main contributions to the (b) true term. (a) and (c) are highly similar, but the negative (c) $\mathbf{EPW}_{(\mathbf{i,iii})}$ divergence in the WB region results from the combination of the barotropic and 1st baroclinic mode, indicating that approximation (ii) biases the interpretation of (a) $\mathbf{EPW}_{(\mathbf{i,ii,iii})}$. (c) and (d) differs, indicating that topographic-interactions are the main contributions to (d) $\mathbf{EPW}_{(\mathbf{i})}$, invalidating approximation (iii).

4.2 Approximation (ii) : contribution of the barotropic mode ($\mathbf{EPW_{(i,ii,iii)}}$ *vs.* $\mathbf{EPW_{(i,iii)}}$)

With approximation (ii) (η field primarily reflecting the 1^{st} baroclinic mode), the mesoscale EKE reservoir – formally represented by the barotropic and 1^{st} baroclinic modes (Wunsch, 2007; Smith & Vallis, 2001; Venaille et al., 2011; Tedesco et al., 2022) – is represented by the 1^{st} baroclinic mode alone. This can lead to a misinterpretation of the dynamics of the mesoscale EKE reservoir. It can gain or loose EKE through the barotropic mode and the barotropic and 1^{st} baroclinic modes can exchange EKE, via barotropisation and scattering processes, without affecting the content of the mesoscale EKE reservoir. The necessity to account for both modes to infer the mesoscale EKE-fluxes divergence is supported by $\mathbf{EPW}$, whose contribution in the WB region (0.81 GW; Figure 2b) results from the partial compensation between the barotropic (1.56 GW) and the 1^{st} baroclinic modes (-0.75 GW) (not shown). It indicates that barotropization is a significant process in the WB region.

The expression of $\mathbf{EPW_{(i,iii)}}$ (Eq. 11) accounts for the different vertical modes using α_n^2 – the vertical partitioning of the variance of η. The η variance mainly partitions into the 1^{st} baroclinic mode (38 $\pm$ 2 %) and more weakly, but still significantly, into the barotropic mode (16 $\pm$ 4 %) (Appendix B). It indicates that the mesoscale EKE reservoir can be formally represented by the barotropic and 1^{st} baroclinic modes using η. The η variance also significantly partitions into an intermodal coupling term (36 $\pm$ 2 %), originating from the modal correlation in time at the surface (Wunsch, 1997). However, the intermodal coupling term does not contribute to $\mathbf{EPW_{(i,iii)}}$ (Eq. 11), because it uses the orthogonality contribution (2) and therefore only accounts for individual vertical modes.

Approximation (ii) is evaluated by comparing $\mathbf{EPW_{(i,ii,iii)}}$ (Figure 2a) with $\mathbf{EPW_{(i,iii)}}$ (Figure 2c). $\mathbf{EPW_{(i,ii,iii)}}$ and $\mathbf{EPW_{(i,iii)}}$ have highly similar patterns and magnitudes across the region. However, the net mesoscale EKE sink in the WB region denoted by $\mathbf{EPW_{(i,iii)}}$ (-0.81 GW; Figure 2c) results from the combination of the barotropic (-0.51 GW) and 1^{st} baroclinic modes (-0.30 GW) (not shown). It is in contrast with the net $\overline{EKE}$ sink denoted by $\mathbf{EPW_{(i)}}$ (-1.10 GW), which was interpreted as primarily due to the 1^{st} baroclinic mode (Figure 2a).
This indicates that both vertical modes need to be accounted to accurately interpret the mesoscale EKE-fluxes divergence. It also indicates that even though the barotropic mode does not dominate the η variance (16 $\pm$ 4 %; Appendix B), it is the dominant contribution to the vertically-integrated $\mathbf{EPW_{(i,iii)}}$ in the WB region.

Approximation (ii) biases the interpretation of $\mathbf{EPW_{(i,ii,iii)}}$ (Eq. 10). However, it is not at the origin of the strong discrepancies between the η-based terms - $\mathbf{EPW_{(i,ii,iii)}}$ (Eq. 10) and $\mathbf{EPW_{(i,iii)}}$ (Eq. 11) - and the true term $\mathbf{EPW}$ (Eq. 4).

4.3 Approximation (iii) : contribution of topographic interactions ($\mathbf{EPW_{(i,iii)}}$ *vs.* $\mathbf{EPW_{(i)}}$)

The WB region is characterized by large topographic variations, having a spatially-averaged magnitude of $O(3\ 10^{-2})$, which can locally peak at $O(6\ 10^{-2})$. This questions the use of approximation of (iii) mesoscale eddies interaction with topography being negligible in the WB region.

Approximation (iii) is evaluated by comparing $\mathbf{EPW_{(i,iii)}}$ (Eq. 11; Figure 2c) against $\mathbf{EPW_{(i)}}$ (Eq. 7; Figure 2d), which includes topographic interactions. The two terms locally differ by their patterns and magnitudes. However, their cumulative contributions in the WB region denote a net mesoscale EKE sink ($\mathbf{EPW_{(i,iii)}}$;$\mathbf{EPW_{(i)}} < 0$). The term including topographic interactions ($\mathbf{EPW_{(i)}}$) has contrasted patterns within the WB region and is the most intense at the Eastern Agulhas Bank Bight (23°E-27°E). The local magnitude of $\mathbf{EPW_{(i)}}$ is larger by an order of magnitude than $\mathbf{EPW_{(i,iii)}}$, which excludes topographic interactions.
Topographic interactions are mainly due to the EKE fluxes-topographic interactions (**C** : -3.05 GW in the WB region, not shown) whereas the β-contribution to topographic interactions have a negligible contribution (**A2** : 0.76 GW in the WB region, not shown).
A valid approximation would be to neglect the β-contribution (**A1**) and the β-contribution to the topographic interactions (**A2**), compared to the EKE fluxes-topographic interactions (**C**).

Approximation (iii) has a significant impact on $\mathbf{EPW_{(i,iii)}}$ (Eq. 11). However, $\mathbf{EPW_{(i)}}$ (Eq. 7), adjusted of approximations (ii) and (iii), is mainly negative in the WB region, consistently with the former version of the η-based term ($\mathbf{EPW_{(i,ii,iii)}}$ in Eq. 10). It indicates that approximations (ii) and (iii) are not the reasons for the opposite signs of the η-based ($\mathbf{EPW_{(i,ii,iii)}}$ in Eq. 10; Figure 2a) and the true (**EPW** in Eq. 4; Figure 2b) eddy-pressure works.

4.4 Approximation (i) : contribution of ageostrophic motions (β-contribution *vs.* ageostrophic EPW)

Approximation (i) (geostrophic velocities) is the last possible reason for the net differences in the WB region between the η-based ($\mathbf{EPW_{(i,iii)}}, \mathbf{EPW_{(i)}} < 0$; Figure 2c,d) and true ($\mathbf{EPW} > 0$; Figure 2b) mesoscale **EPW**. It suggests that the main contribution to **EPW** is the ageostrophic part of mesoscale eddies velocity.

We use a scale analysis to explain the prevalence of ageostrophy ($\mathbf{u}'_{ag,n}$; $p'_{ag,n}$), in relation with the β-contribution (subterm in $\mathbf{EPW_{(i)}}$ Eq. 7 and $\mathbf{EPW_{(i,iii)}}$ Eq. 11), for the true **EPW** (Eq. 4). We focus here on the β-contribution only, because it was the one investigated as the main contribution to **EPW** by Zhai et al. (2010). We derive the scale analysis for a purely ageostrophic ($\mathbf{u}'_{ag,n}$; $p'_{ag,n}$ in Eq. 12) and a partially ageostrophic ($\mathbf{u}'_{ag,n}$; $p'_{g,n}$ in Eq. 13) **EPW**. It allows to account for the different possible contributions of the ageostrophic part of mesoscale eddy velocity to the true **EPW**.

$$\left|\int_{-H}^{\eta} \nabla_H \cdot \left(\mathbf{u}'_{ag,n} p'_{ag,n} \phi_n^2\right)\, dz\right| \sim \frac{Ro^2 U'_g P'_g H}{L} \tag{12}$$

$$\left|\int_{-H}^{\eta} \nabla_H \cdot \left(\mathbf{u}'_{ag,n} p'_{g,n} \phi_n^2\right)\, dz\right| \sim \frac{Ro U'_g P'_g H}{L} \tag{13}$$

$$\left|\frac{\beta \rho_0 g^2}{2f^2} \int_{H}^{\eta} \frac{\partial}{\partial_x} \left(\frac{\phi_n^2}{|\phi_n^2|_{z=0}} \alpha_n^2 \eta'^2\right)\, dz\right| \sim \frac{\widehat{\beta} P' U'_g H}{\widehat{f}} \tag{14}$$

$$\frac{(12)}{(14)} = \frac{Ro^2 \widehat{f}}{L\widehat{\beta}} = \frac{L_{cross-over}}{L}, \text{ with } L_{cross-over} = \frac{Ro^2 \widehat{f}}{\widehat{\beta}} \tag{15}$$

$$\frac{(13)}{(14)} = \frac{Ro \widehat{f}}{L\widehat{\beta}} = \frac{L_{cross-over}}{L}, \text{ with } L_{cross-over} = \frac{Ro \widehat{f}}{\widehat{\beta}} \tag{16}$$

with $|\nabla_H, \frac{\partial}{\partial_x}| \sim \frac{1}{L}$, $|\int_{-H}^{\overline{\eta}} <.> dz| \sim H$, $|\beta| \sim \widehat{\beta}$, $|f| \sim \widehat{f}$, $|\mathbf{u}'_{ag,n}| \sim RoU'_g$ and $|p'_{ag,n}| \sim RoP'_g$ using the expansion of velocity and eddy pressure with $Ro = \frac{U'}{\widehat{f}L}$ the small parameter, $|p'_{g,n}| \sim P'_g \sim \rho_0 \widehat{f} U'_g L$ using geostrophy and $\left|\frac{\phi_n^2 \alpha_n^2 \eta'^2}{|\phi_n^2|_{z=0}}\right| \sim \frac{P'_g U'_g L \widehat{f}}{\rho_0 g^2}$ using hydrostatic and geostrophy.

The scale analysis leads to the definition of a cross-over scale ($L_{cross-over}$ in Eq. 15 and 16) marking the transition from an ageostrophic-dominated **EPW** ($L_{cross-over} >> L_{eddy}$) to a β-contribution dominated **EPW** ($L_{cross-over} << L_{eddy}$). $L_{cross-over}$ varies with the ratio $\frac{\widehat{f}}{\widehat{\beta}}$ modulated by the Rossby number of mesoscale eddies Ro ($Ro = \frac{\frac{1}{H}\int_{-H}^{\eta} ||\mathbf{u'_{0-1}}||\, dz}{|f| L_{eddy}}$, with $L_{eddy} = Rd = O(35)$ km the lower bound of the characteristic horizontal scale of mesoscale eddies in the WB region).
The ratio $\frac{f}{\beta}$ has the dimension of a scale and is supposed to be large in a β-plan at mid-latitudes. Its spatially-averaged value in the WB region is 4200 $\pm$ 395 km.
Ro is a measure of ageostrophy relative to geostrophy (Cushman-Roisin & Beckers, 2011). The typical Ro range of values for mesoscale eddies at mid-latitudes inferred from satellite altimetry data ($O(< 0.05)$ from Chelton et al. (2011)) is used as a reference for mesoscale eddies in the WB region. Ro has a contrasted distribution in the WB region (Figure 3a). 70 % of its values are in the range O(0.025 - 0.055) and the rest of the values are larger O(0.1-0.5) and located at the Agulhas Current inner front. It confirms that mesoscale eddies are mainly geostrophic in most of the WB region. They are more ageostrophic at the inner front where the velocity shear is more intense and where they likely interact with topography.

The main contribution to the true **EPW** in the WB region takes the form of a partially ageostrophic **EPW**. $L_{cross-over}$ – defined in Eq. 16 – has values in the range O(110-220) km in 70 % of the WB region, with larger values located at the inner front of the Agulhas Current (Figure 3b). It results in L_{eddy} (O(35-100) km) falling in the range of a partially ageostrophic-dominated **EPW**, relative to the β-contribution ($L_{cross-over} \sim O(1-7)L_{eddy}$), in the WB region. The purely ageostrophic **EPW** has a weaker contribution to the true **EPW** than the β-effect in most of the WB region. $L_{cross-over}$ – defined in Eq. 15 – has values in the range O(3-10) km in 70 % of the WB region, with larger values ($> O(110)$ km) located at the inner front of the Agulhas Current (not shown). This results in $L_{cross-over} \sim O(10^{-1} - 10^{-2})L_{eddy}$ in most of the WB region.

Although geostrophy is a good approximation for mesoscale eddies velocity in most of the WB region ($Ro = O$(0.025-0.055); Figure 3a), the purely geostrophic **EPW** (Figures 2c,d) is not the main contribution to the true **EPW** (Figures 2b). The geostrophic part of the linear EKE-fluxes reduces to a β-contribution, because the divergence of the geostrophic flow cancels out (Eq. 7). The scale analysis (Eq. 16) indicates that for the mesoscale regime

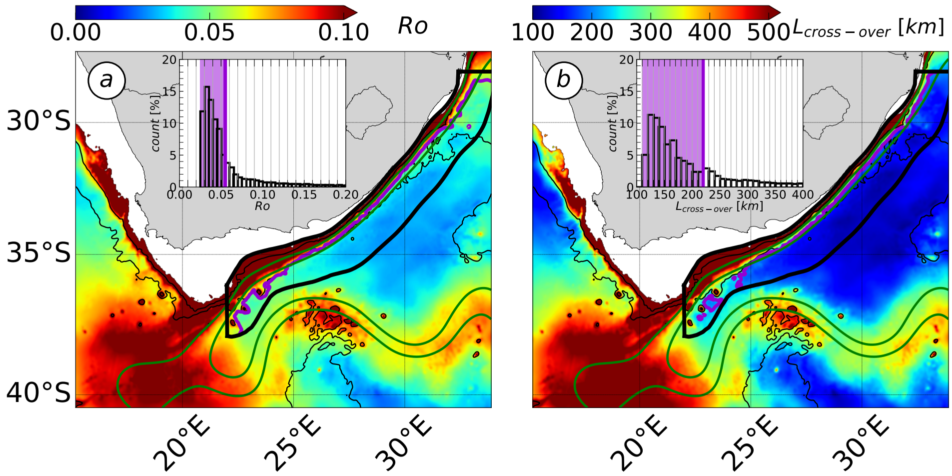

Figure 3: (a) Rossby number of mesoscale eddies ($Ro = \frac{\frac{1}{H}\int_{-H}^{\eta} ||\mathbf{u}'_{0-1}|| \ dz}{|f|L_{eddy}}$) and (b) cross-over scale ($L_{cross-over} = \frac{Ro|f|}{\beta}$ in Eq. 16) [km] defined by the scaling analysis using a partially ageostrophic **EPW**. The purple lines denote Ro and $L_{cross-over}$ isolines of 70 % percentiles, the green contours denote the 0.25 m and 0.5 m isolines of η and black contours denote the 1000 m and 3000 m isobaths. The terms count in the WB region [%] are shown as barplots, where shaded areas denote the range of values of the 70 % percentile (purple lines). (a) Ro shows that mesoscale eddies are mainly geostrophic in the WB region (O(0.025-0.055) in 70 % of the WB region). However, (b) $L_{cross-over} >> L_{eddy}$ (with $L_{eddy} = O$(35-100) km), confirming the prevalence of partially **EPW**, relative to the β-contribution, to the true **EPW**.

in the WB region, the contribution of coupled geostrophic (pressure) and ageostrophic (velocity) components of mesoscale eddy dominates the β-contribution ($L_{cross-over} >> L_{eddy}$). Approximation (i) therefore questions the use of satellite altimetry data to infer **EPW** (Eq. 5).

Our results about **EPW** do not allow to draw conclusion on the use of satellite altimetry data to infer **AEKE**, the other component of the mesoscale EKE-fluxes divergence. Another relevant metric to measure the β-contribution to dynamical regimes in quasi-gesotrophic balance is the Rhines scale, $L_{Rh} = \sqrt{\frac{U'}{\beta}}$, (Rhines, 1975). The scale marks the transition from a Rossby waves-dominated variability, corresponding to the β-effect ($L_{Rh} << L_{eddy}$), to a nonlinear eddy-dominated variability ($L_{Rh} >> L_{eddy}$).
L_{Rh} has values in the range O(65-90) km in 70 % of the WB region, with larger values located at the inner front of the Agulhas Current (Appendix C). It results in L_{eddy} to rather fall in the range of nonlinear eddy-dominated variability ($L_{Rh} \sim O(0.65-3)L_{eddy}$) in the WB region. The L_{Rh} metric broadens the weak β-contribution in the WB region, that we asserted for the EKE-fluxes divergence, to the mesoscale variability. L_{Rh} also shows that the mesoscale variability in the WB is dominated by nonlinear eddy, suggesting that **AEKE** (non-linear component) has a larger contribution to the EKE-fluxes divergence than **EPW** (linear component).
In order to conclude on the use of satellite altimetry data to infer the EKE-fluxes diver-

gence, we assess in the following section the impact of the geostrophic approximation (i) on the **AEKE** term.

5 Results II : Main contributions to the true AEKE

In this section we evaluate the η-based estimation of **AEKE** ($\mathbf{AEKE_{(i)}}$ in Eq. 8). We first evaluate if $\mathbf{AEKE_{(i)}}$ is a reliable approximation of **AEKE** (Eq. 4). We then furtherly characterize the main contributions to the true **AEKE**.

5.1 Comparison between the approximated $\mathbf{AEKE_{(i)}}$ and the true AEKE

$\mathbf{AEKE_{(i)}}$ and **AEKE** are in fairly good agreement over the region (Figure 4a,b). They are both mainly positive in the WB region, supporting the WB being a region of mesoscale eddy generation, whose energy is then exported. Their contributions are mainly significant along the southern Agulhas Current branch (downstream of Port Elizabeth), where mesoscale variability is high. They show the largest net mesoscale EKE source at the Eastern Agulhas Bank Bight, which spreads almost uniformly across the width of the WB region. The cumulated $\mathbf{AEKE_{(i)}}$ over the WB region amounts to 73 % of **AEKE**. The difference in magnitude between the two terms is explained by the presence of a large sink at the Eastern Agulhas Bank Bight Tip (22°E - 23°E) visible in $\mathbf{AEKE_{(i)}}$.
The fairly good qualitative and quantitative agreements between $\mathbf{AEKE_{(i)}}$ and the true **AEKE** indicate that the η-based term accounts for the main contribution to **AEKE**. This suggests that geostrophic flows are the main contributions to **AEKE**, contrary to **EPW**.

On a separate note, both terms result from a combination of the barotropic ($\mathbf{AEKE_{(i)}}$: 0.57 GW ; **AEKE** : 0.88 GW, not shown) and 1st baroclinic modes ($\mathbf{AEKE_{(i)}}$: 1.10 GW ; **AEKE** : 1.41 GW, not shown). It confirms the need to account for both vertical modes to accurately infer the mesoscale EKE-fluxes divergence in the WB region.

In the following subsection, we characterize in details the contribution of each subcomponents – β-contribution (**A** in Eq. 8), work of eddy-total flow interactions (**B** in Eq. 8) and EKE fluxes-topographic interactions (**C** in Eq. 8) – to $\mathbf{AEKE_i}$ (Eq. 8).

5.2 Approximation (i) : contribution of geostrophic motions to the true AEKE

The contribution of the work of eddy-total flow interactions (**B** in Figure 4d) represents the main contribution to $\mathbf{AEKE_{(i)}}$ (Figure 4a), while the β-contribution (**A** in Figure 4c) have a weaker and opposite contribution.

The work of eddy-total flow interactions (**B** in Eq. 8) is a reliable estimate of the net mesoscale EKE source in the WB region denoted by $\mathbf{AEKE_{(i)}}$ (up to 73 %) and by **AEKE** (up to 53 %).
The β-contribution (**A** in Eq. 8) is almost uniformly negative in the WB region and amounts to a net mesoscale EKE sink of magnitude O(-0.19) GW. **A** (Eq. 8) is the non-linear counterpart of the β-contribution to **EPW** (**A** term in Eq. 7). Both β-contributions have similar contributions to the EKE-fluxes divergence (Figures 2c and 4c), although the non-linear β-effect has a weaker cumulative contribution in the WB region (-0.19 GW; Figure 4c) than the linear β-effect (-0.81 GW; Figure 2c).
The cumulative contribution of EKE fluxes-interactions with topography (**C** in Eq. 8) in the WB region is 0.65 GW (not shown). It is weaker than that the one of the work of eddy-total flow interactions (**B**), but remains significant. It confirms the need to account for topographic interactions to accurately infer the net mesoscale EKE sources and sinks in the WB region.

The geostrophic approximation is valid to estimate the true **AEKE**, contrary to **EPW**. It enables the use of η to qualitatively infer the **AEKE** component of the mesoscale EKE-fluxes divergence.

6 Conclusion on the η-based EKE-fluxes divergence

In this section, we draw a conclusion on the use of η to infer the EKE-fluxes divergence, based on our results for its **EPW** (cf. section 4) and **AEKE** components (cf. section 5).

The EKE-fluxes divergence denotes a net mesoscale EKE source in the WB region (**EPW** > 0 in Figure 2b; **AEKE** > 0 in Figure 3b). It in the WB region (3.10 GW) is primarily due to **AEKE** (2.29 GW) and more weakly to **EPW** (0.81 GW). The net mesoscale EKE source supports the WB as a region of mesoscale eddies generation.

AEKE corresponds to the advection of EKE by the total flow. It significantly exports EKE along the southern Agulhas Current branch (**AEKE** > 0), where mesoscale variability is high (Figure 4b). **AEKE** primarily accounts for the transport done by geostrophic EKE-fluxes (73 % in the WB region; Figure 4a), in the form of the work of eddy-total flow interactions (53 % in the WB region; Figure 4d).
EPW represents EKE transport done by the linear part of variability, usually interpreted as the wave dynamics. The EKE export along the southern current branch (**EPW** > 0), where mesoscale variability is high, dominates the **EPW** cumulated contribution in the WB region. **EPW** primarily accounts for the EKE transport done by coupled geostrophic-ageostrophic EKE-fluxes. It is explained by a scaling analysis (Eq. 16), which indicates that the predominance of the geostrophic-ageostrophic **EPW**, over the geostrophic one – reducing to the β-effect – is due to the ratio $\frac{Ro|f|}{\beta}$ being larger than typical scale of mesoscale eddies in the WB region.

The geostrophic approximation is required by the use of η and is the most critical approximation to infer the EKE-fluxes divergence. In the WB region, the approximation is valid for the **AEKE** component, which dominates the EKE-fluxes divergence. The use of η to infer the EKE-fluxes divergence therefore leads to a fairly good qualitative degree of accuracy, but it significantly underestimates its magnitude in the WB region (26 %).

Approximation (ii) (η primarily reflecting the 1^{st} baroclinic mode) and (iii) (topographic interactions being negligible) are less critical, but significantly bias the interpretation and accuracy of the EKE-fluxes divergence.
Both approximations are not directly required by the use of η field and can potentially be relaxed using other datasets in addition to satellite altimetry data. Numerical outputs and bathymetry data would respectively be needed to derive η partitioning between vertical modes (approximation (ii)) and the contribution of the EKE fluxes-topographic interactions (approximation (iii)).

7 Summary and Discussion

7.1 Summary

We have assessed the mesoscale EKE-fluxes divergence and the use of sea surface height (η) to infer it, using a numerical simulation of the Agulhas Current region. The η-based EKE-fluxes divergence is a reliable qualitative estimate of the true one (54 %), via one of its component – the advection of EKE by the total flow (**AEKE**; Figure 4).
It is in favor of the use of satellite altimetry data to infer the net mesoscale EKE sources and sinks in the region of the Agulhas Current and especially in favor of the upcoming SWOT mission (Morrow et al., 2019; d'Ovidio et al., 2019). Although scales $< O(100)$ km do not significantly contribute to $\mathbf{EPW}_{\mathbf{(i,ii,iii)}}$ (Eq. 10; Figure 1) – corresponding to the β-contribution – it may not be the same for $\mathbf{AEKE}_{\mathbf{(i)}}$ (Eq. 8) accounting for others contributions. With an effective resolution (15-30 km) comparable to the one of our numerical

simulation (25 km following Soufflet et al. (2016)), the SWOT mission would likely allow to infer an EKE-fluxes divergence with an accuracy close to that of our regional numerical simulation.

7.2 Discussion

Our study supports the WB region of the Agulhas Current as a hotspot of mesoscale eddy generation, whose energy is then exported (EKE-fluxes divergence > 0; Figures 2b and 4b). It is in contrast with the paradigm of remotely-generated mesoscale eddy decay at WB regions (EKE-fluxes divergence < 0) due to direct EKE routes channeled by topography (Zhai et al., 2010; Chelton et al., 2011; Evans et al., 2020; Z. Yang et al., 2021; Evans et al., 2022).
The latter paradigm relies on the β-effect being the main contribution to the EKE-fluxes divergence (Zhai et al., 2010). Our analysis of the main contributions to the EKE-fluxes divergence show that the β-contribution is weak in the WB region for the mesoscale regime, explaining the different paradigms. The weak β-contribution is inferred from a scale analysis ($L_{cross-over}$ Eq. 16) and the Rhines scale (L_{Rh} in Appendix C). $L_{cross-over}$ is larger than the typical scale of mesoscale eddies (L_{eddy}) in the WB region, resulting in a dominating coupled geostrophic-ageostrophic **EPW** relative to the β-effect. L_{Rh} is larger than L_{eddy}, resulting in nonlinear eddy-dominated mesoscale variability – corresponding to the **AEKE** components of the EKE-fluxes divergence – relative to the β-effect.
$L_{cross-over}$ and L_{Rh} denote the sensitivity of the EKE-fluxes divergence contributions to the regional mesoscale dynamics. Both metrics vary across latitudes, within western boundary regions, and across oceanic gyres. They can possibly point toward reversed main contributions to the EKE-fluxes divergence. The paradigm of remotely-generated mesoscale eddy decay may therefore be valid in specific oceanic regions.

The leading-order processes of the mesoscale EKE-budget at western boundary regions allow to further interpret the mesoscale EKE-fluxes divergence.
In the Agulhas Current region, a study showed that the mainly positive mesoscale EKE-fluxes divergence results from the local generation of EKE, by instability processes of the current, overcoming the local EKE decay by topographically-channeled interactions and dissipation due to bottom-friction and wind (Tedesco et al., 2022). It is in contrast with studies in a mid-latitude WB region, without a western boundary current, which showed that remotely-generated mesoscale eddies decay due to a zoo of topographically-channeled processes triggering direct EKE routes (Evans et al., 2020, 2022). In the same way, a study based on an idealized WB region and without a mean current, showed a mesoscale eddies decay due to topographically-channeled turbulence, in the presence of rough topography (Z. Yang et al., 2021).
The studies suggest that the EKE-fluxes divergence varies within western boundary regions, due to the presence of a western boundary current. In the presence of an intense mean current, the local generation of EKE may overcome the local decay, while in the absence of intense generation processes, the local EKE decay may dominate.

In a nutshell, the different studies suggest that western boundary regions would be the place of contrasted mesoscale EKE-fluxes divergence, depending on regional factors. However, the validity of our discussion in the context of other WB regions is to consider cautiously, as the different studies are based in different western boundary regions and use different methods. It would require additional studies of other western boundary regions, including or excluding a current, to conclude on the western boundary regions dynamics and their contributions to the global ocean energy budget.
Some elements of response on mesoscale eddy dynamics upon western boundaries at a global scale can be found using numerical simulations (Qiu et al., 2018; Torres et al., 2018). The

SWOT mission presents the potential to test on a global scale the suggestion that western boundaries have contrasted contributions to the global ocean energy budget.

Appendix A Sensitivity of EPW to spatial smoothing

The true **EPW** (Eq. 4) is spatially smoothed to emphasize the large-scale patterns driving its cumulative contribution in the WB region.
The unsmoothed **EPW** term is characterized by small-scales patterns that are the most intense at topographic features – shelf slope (1000 m isobath), seamounts, canyons, roughness, etc – locally peaking at $O(2.5 - 10)$ W m^{-2} (Figure A1a). The intense small-scales patterns are larger of an order of magnitude than the unsmoothed $\mathbf{EPW}_{\mathbf{(i,ii,iii)}}$ term in the WB region (O(0.001-0.1) W m^{-2}; Figure 2a). However, **EPW** has a cumulative contribution in the WB region (1.31 GW; Figure A1a) of close magnitude than the one of $\mathbf{EPW}_{\mathbf{(i,ii,iii)}}$ (-1.33 GW; Figure 2a), regardless of the intense small-scale patterns. It indicates that the intense small-scale patterns locally compensate and do not significantly contribute to the **EPW** cumulative contribution in the WB region.

The sensitivity of the true **EPW** (Eq. 4) to the smoothing is shown using a Gaussian kernel of progressively increasing length scale : from 35 km, the spatially-averaged *Rd* over the dx $\sim$ 2.5 km grid, to 50 km and to 75 km, two typical mesoscale eddies radii at mid-latitudes as inferred from satellite altimetry (Chelton et al., 2011) (Figure A1). While the patterns of **EPW** significantly change with the different smoothing length scales, the order of magnitude of the cumulative contribution in the WB is fairly unchanged.
In the Figures of the present study, the label 'smoothed' refer to the Gaussian kernel using a 75 km-radius. Both smoothings using 50 km- and 75 km-radius result in fairly close cumulative **EPW** contributions in the WB region (Figures A1c,d). The 75 km-radius smoothing provides smoother patterns, emphasizing the most the large-scale patterns driving the **EPW** cumulative contribution in the WB region and easing the most its comparison with $\mathbf{EPW}_{\mathbf{(i,ii,iii)}}$ (Eq. 10).

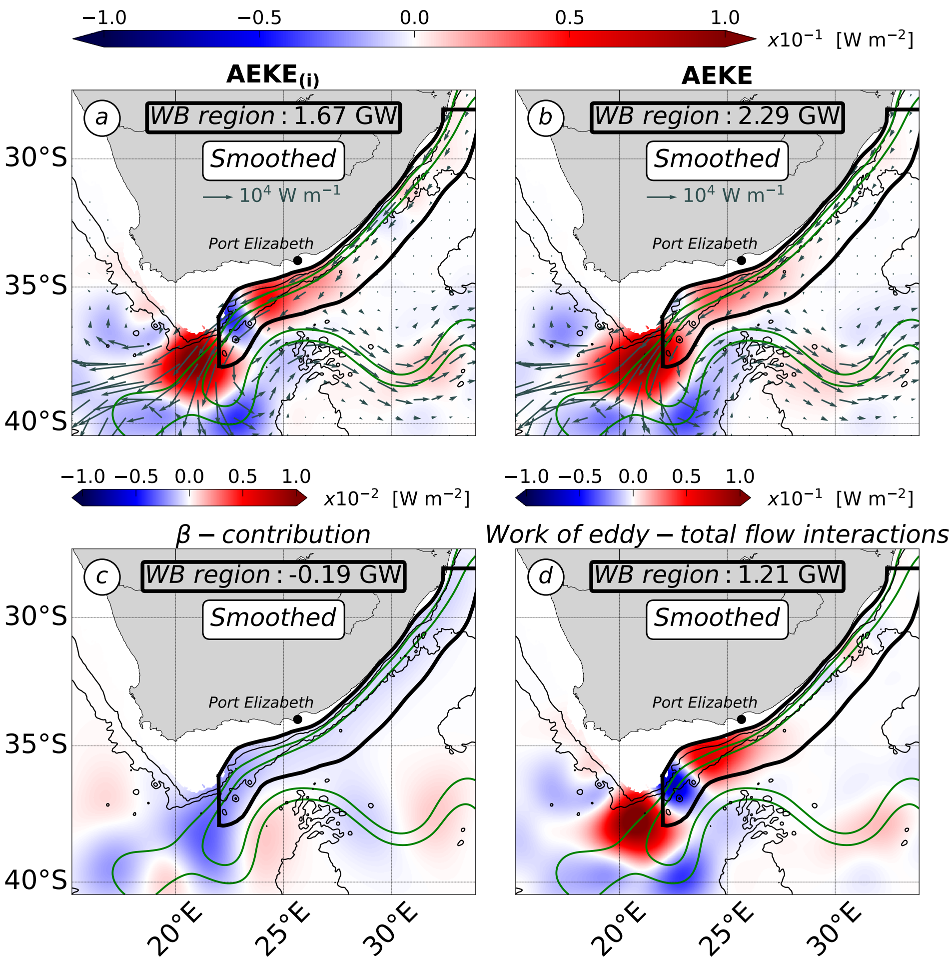

Figure 4: (a) $\mathbf{AEKE_{(i)}}$ (Eq. 8 for $n = 0-1$), (b) **AEKE** (Eq. 6 for $n = 0-1$), the contributions to $\mathbf{AEKE_{(i)}}$ of (c) the β-effect (**A** in Eq. 8) and of (d) the work of the eddy-total flows interactions (**B** in Eq. 8) [W m^{-2}]. (a,b) Vector fields denote the non-linear EKE_{0-1}-fluxes ($\frac{\rho_0}{2}\int_{-H}^{\eta} \mathbf{u}_{0-1}\phi_{0-1}||\mathbf{u}'_{0-1}\phi_{0-1}||^2\, dz$) using respectively the geostrophic ($\mathbf{u}_n\phi_n = \mathbf{k} \wedge \frac{g}{f}\nabla_H \left(\frac{\phi_n}{|\phi_n|_{z=0}}\lambda_n \eta\right)$ with $\lambda_n = \frac{\eta_n}{\eta}$) and total velocity fields ($\mathbf{u}_n\phi_n$) [W m^{-1}]. Note the magnitude difference between (c) and (a,b,d). cf. Figure 2 for a detailed caption. (a) $\mathbf{AEKE_{(i)}}$ accounts for the main contributions of (b) the true **AEKE**, via (d) the work of geostrophic eddy-total flows interactions.

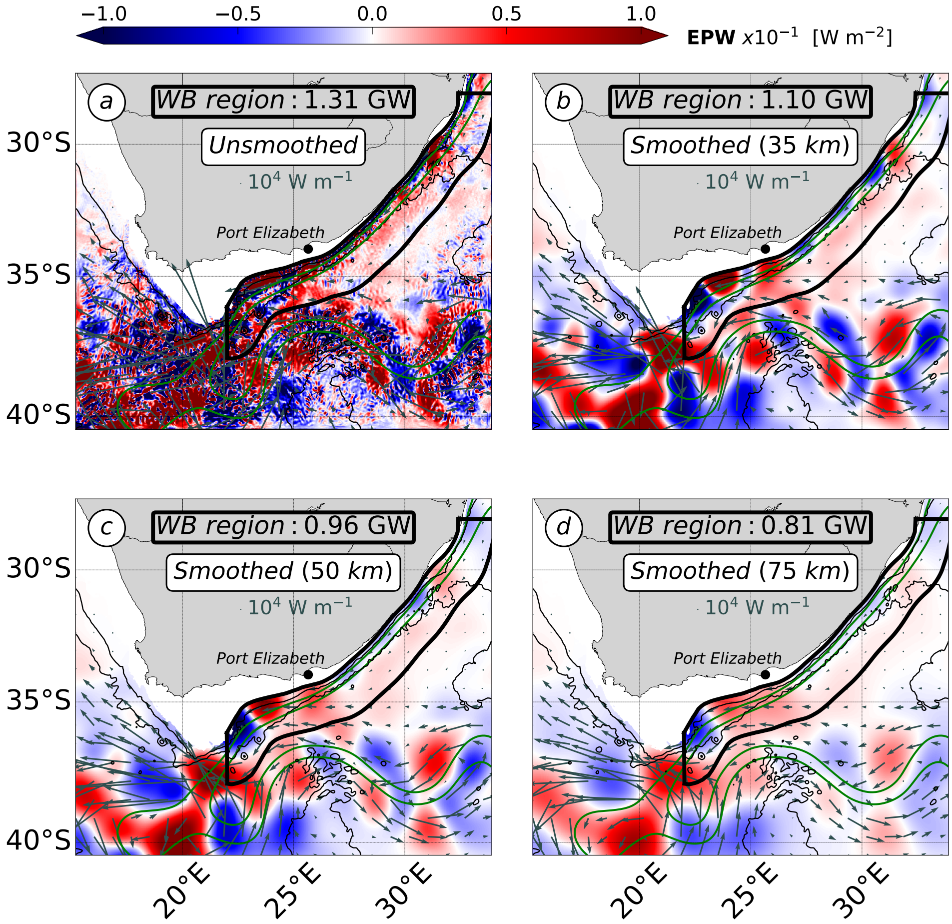

Figure A1: The true **EPW** (Eq. 5 for $n = 0-1$) [W m^{-2}] (a) unsmoothed and smoothed with a Gaussian kernel of (b) 35 km-, (c) 50 km- and (d) 75 km-radius. Vector fields denote the corresponding linear EKE_{0-1}-fluxes ($\int_{-H}^{\eta} \mathbf{u}'_{0-1} p'_{0-1} \phi 0-1^2 \ dz$) [W m^{-1}]. cf. Figure 2 for a detailed caption. (d) The 75 km-radius smoothing length scale, a typical value of mesoscale eddy radius at mid-latitudes (Chelton et al., 2011), emphasizes the large-scale patterns driving the cumulative contribution of **EPW** in the WB region and eases its comparison with $\mathbf{EPW}_{(\mathbf{i},\mathbf{ii},\mathbf{iii})}$ (Eq. 10).

Appendix B Partitioning of η variance between the barotropic and 9 first baroclinic modes

The partitioning of the η variance (η'^2) between the vertical modes (α_n^2) is used to define $\mathbf{EPW}_{\mathbf{(i,iii)}}$ (Eq. 11), an adjusted expression of $\mathbf{EPW}_{\mathbf{(i,ii,iii)}}$ (Eq. 10), in order to evaluate approximation (ii) of η field primarily reflecting the 1^{st} baroclinic mode (section 2.1.3.2).
We limit our analysis to the barotropic and 9 first baroclinic modes which capture 85-100 % of the modeled η'^2 in the Agulhas Current region (not shown). η is a 2D field and cannot be projected on the vertical mode base ϕ_n, but the η modal coefficient (η_n) is inferred using the relation $|p|_{z=0} = \rho_0 g \eta$, as follows : $\eta_n = \frac{1}{\rho_0 g} \frac{p_n}{|\phi_n|_{z=0}}$. The modal expression of η'^2 is derived and α_n^2 are defined as follows :

$$\eta'^2 = \sum_{n=0}^{\infty} \eta'_n \sum_{m=0}^{\infty} \eta'_m = \sum_{n=0}^{\infty} \eta_n'^2 + \underbrace{\sum_{n=0}^{\infty} \sum_{m \neq n}^{\infty} \eta'_n \eta'_m}_{Intermodal\ coupling\ (C_{nm})} = \sum_{n=0}^{\infty} \eta_n'^2 + C_{nm} \tag{B1}$$

$$\alpha_n^2 = \frac{\eta_n'^2}{\eta'^2} \ ; \ \alpha_{nm} = \frac{C_{nm}}{\eta'^2} \tag{B2}$$

The modal expression of η'^2 involves an intermodal coupling term C_{nm} (B1). It corresponds to a phase-locked combination of vertical modes due to the modal correlation in time at the surface (Wunsch, 1997; Scott & Furnival, 2012). The degree of the modeled modal correlation at the surface ($\frac{\sum_{n=0}^{9} \eta_n'^2}{\sum_{n=0}^{9} \eta_n'^2 + C_{nm}}$) is 1.8 in average in the Agulhas Current region, which is consistent with the 2-3 factor determined from *in situ* data at global-scale by Wunsch (1997). It must be noted that the true **EPW** (Eq. 5) implies the orthogonality condition (resulting in canceling out the C_{nm} term) and that it therefore only accounts for the contributions of the individual vertical modes categories ($n = 0$ and $n = 1$).

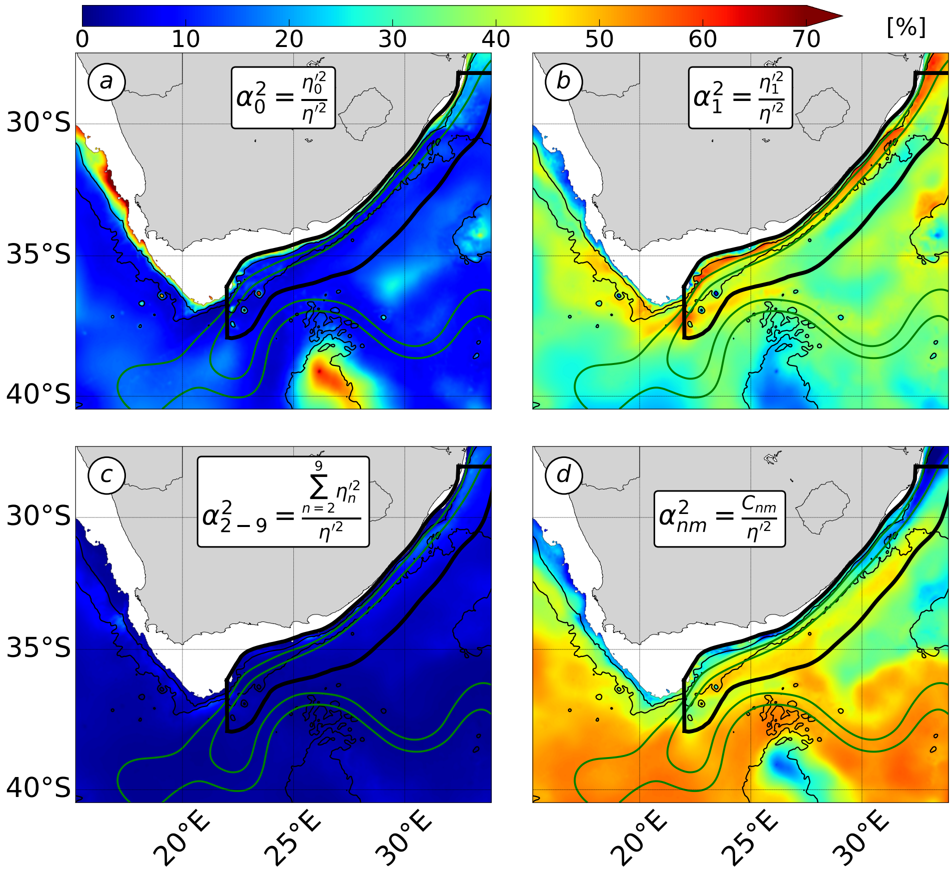

Figure B1: Partitioning of η variance (α_n^2) between the vertical modes categories : (a) $n = 0$, (b) $n = 1$, (c) $n = 2 - 9$ and (d) the intermodal coupling term $\overline{C_{nm}}$ [%] (B1). (cf. Figure 2 for a detailed caption). The η variance largely partitions into (b) the 1^{st} baroclinic mode and more weakly into (a) the barotropic mode, which both contribute to $\mathbf{EPW}_{i,iii}$ (Eq. 11).

η'^2 mainly partitions into the individual 1^{st} baroclinic mode (38 ± 2 % in the WB region) and the intermodal coupling term (36 ± 2 % in the WB region). It also partitions more weakly, but still significantly into the individual barotropic mode (16 ± 4 % in the WB region) (Figure B1). The partitioning of η'^2 is partially consistent with the usual interpretation of η primarily reflecting the 1^{st} baroclinic mode (Wunsch, 1997; Smith & Vallis, 2001). However, it indicates that the vertical structure of mesoscale eddies – formally represented by the combination of the barotropic ($n = 0$) and 1^{st} baroclinic modes ($n = 1$) (Wunsch, 2007; Smith & Vallis, 2001; Venaille et al., 2011; Tedesco et al., 2022) – can be accurately inferred from η field.

Appendix C Mesoscale variability regime in the WB region by the Rhines scale

The Rhines scale (L_{Rh}) is used to get a measure of the β-contribution to the mesoscale variability in the WB region. L_{Rh} marks the transition from a variability dominated by Rossby waves, corresponding to the β-effect ($L_{Rh} << L$), to a variability dominated by nonlinear eddies ($L_{Rh} >> L$) (Rhines, 1975).

We derive a L_{Rh} for mesoscale eddies as follows : $L_{Rh} = \frac{\frac{1}{H}\int_{-H}^{\eta} ||\mathbf{u'_{0-1}}||\ dz}{\beta}$. L_{Rh} has values in the range O(65-90) km in 70 % of the WB region, with larger values located at the inner front of the Agulhas Current (Figure C1). It results in L_{eddy} (O(35-100) km) to rather fall in the range of nonlinear eddy-dominated variability in the WB region ($L_{Rh} \sim O(0.65-3)L_{eddy}$).
Our scale analysis (Eq. 16) has shown the weak β-contribution to the true **EPW** – linear component of the EKE-fluxes divergence – in the WB region (Figure 3) and L_{Rh} broadens the weak β-contribution to the mesoscale variability. L_{Rh} shows that mesoscale variability is dominated by nonlinear eddy in the WB region, suggesting that **AEKE** (non-linear component) has a larger contribution to EKE-fluxes divergence than **EPW** (linear component). The impact of the geostrophic approximation (i) on **AEKE** must be assessed to be able to conclude on the use of satellite altimetry data to infer the EKE-fluxes divergence.

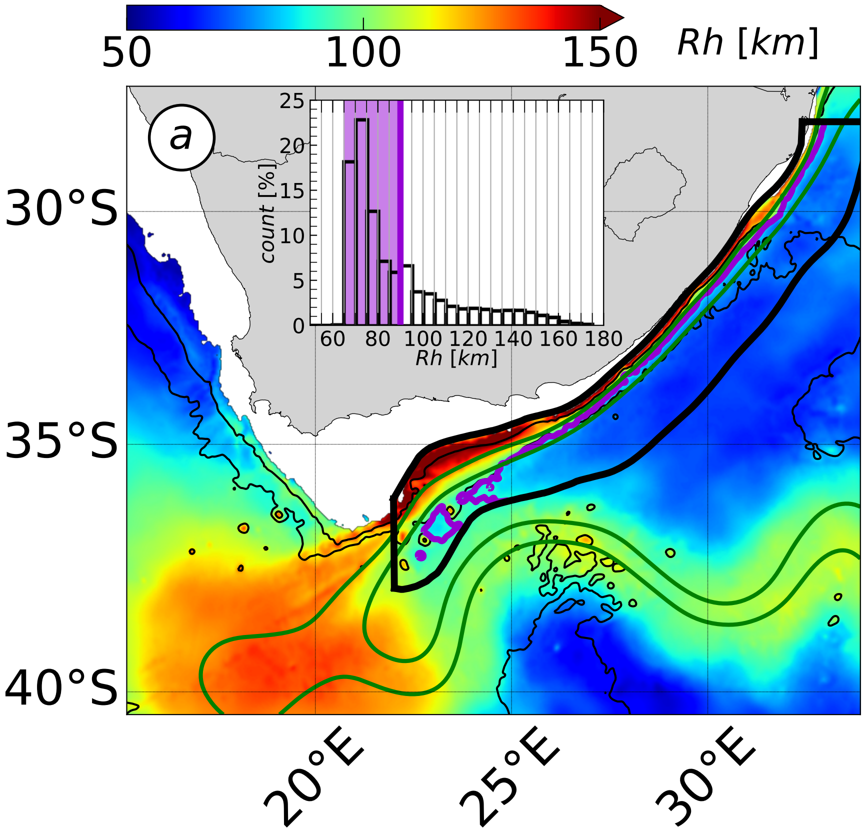

Figure C1: (a) Rhines scale for mesoscale eddies ($L_{Rh} = \sqrt{\frac{\frac{1}{H}\int_{-H}^{\eta} ||\mathbf{u}'_{0-1}||\ dz}{\beta}}$) [km]. The purple lines denote L_{Rh} isoline of 70 % percentile, the green contours denote the 0.25 m and 0.5 m isolines of η and black contours denote the 1000 m and 3000 m isobaths. The terms count in the WB region [%] is shown as barplot, where shaded areas denote the range of values of the 70 % percentile (purple line). (a) $L_{Rh} \sim O(0.65-3)L_{eddy}$ (with $L_{eddy} = O$(35-100) km), indicating that mesoscale variability is rather dominated by non-linear eddies, relative to β-effect, in the WB region. This suggests that **AEKE** (non-linear component) has a larger contribution to EKE-fluxes divergence than **EPW** (linear component).

Acknowledgments

This work was granted access to the HPC resources of IDRIS under the allocation A0040107630 made by GENCI at Paris, France, and of the HPC facilities DATARMOR of "Pôle de Calcul Intensif pour la Mer" at Ifremer, Brest, France. This work was supported by the Ifremer and the Brittany region for PhD funding. WOES36 model outputs are available online at `http://dap.saeon.ac.za/thredds/catalog/SAEON.EGAGASINI/2019.Penven/DAILY_MEANS/1_36_degree/catalog.html` (DOI: 10.15493/SAEON.EGAGASINI.10000096). The AVISO data are available at `www.aviso.altimetry.fr`, the WOA18 and WOCE climatologies are available at `www.nodc.noaa.gov/OC5/woa18/` and `https://icdc.cen.uni-hamburg.de/thredds/catalog/ftpthredds/woce/catalog.html`.

References

Adcock, S., & Marshall, D. (2000). Interactions between geostrophic eddies and the mean circulation over large-scale bottom topography. *Journal of physical oceanography*, *30*(12), 3223–3238.

Capó, E., Orfila, A., Mason, E., & Ruiz, S. (2019). Energy conversion routes in the western mediterranean sea estimated from eddy–mean flow interactions. *Journal of Physical Oceanography*, *49*(1), 247–267.

Charney, J. G. (1971). Geostrophic turbulence. *Journal of the Atmospheric Sciences*, *28*(6), 1087–1095.

Chelton, D., Deszoeke, R., Schlax, M., El Naggar, K., & Siwertz, N. (1998). Geographical variability of the first baroclinic Rossby radius of deformation. *Journal of Physical Oceanography*, *28*(3), 433–460.

Chelton, D., Schlax, M., & Samelson, R. (2011). Global observations of nonlinear mesoscale eddies. *Progress in oceanography*, *91*(2), 167–216.

Chelton, D., Schlax, M., Samelson, R., & de Szoeke, R. (2007). Global observations of large oceanic eddies. *Geophysical Research Letters*, *34*(15).

Chen, R., Flierl, G., & Wunsch, C. (2014). A description of local and nonlocal eddy–mean flow interaction in a global eddy-permitting state estimate. *Journal of Physical Oceanography*, *44*(9), 2336–2352.

Cushman-Roisin, B., & Beckers, J.-M. (2011). *Introduction to geophysical fluid dynamics: physical and numerical aspects.* Academic press.

Debreu, L., Marchesiello, P., Penven, P., & Chambon, G. (2012). Two-way nesting in split-explicit ocean models: Algorithms, implementation and validation. *Ocean Modelling*, *49-50*, 1-21.

Ducet, N., Traon, P.-Y. L., & Reverdin, G. (2000). Global high-resolution mapping of ocean circulation from TOPEX/Poseidon and ERS-1 and-2. *Journal of Geophysical Research: Oceans*, *105*(C8), 19477–19498.

d'Ovidio, F., Pascual, A., Wang, J., Doglioli, A., Jing, Z., Moreau, S., ... others (2019). Frontiers in Fine-Scale in situ Studies: Opportunities During the SWOT Fast Sampling Phase. *Frontiers in Marine Science*, *6*, 168.

Elipot, S., & Beal, L. M. (2015). Characteristics, Energetics, and Origins of Agulhas Current Meanders and Their Limited Influence on Ring Shedding. *Journal of Physical Oceanography*, *45*(9), 2294-2314. doi: 10.1175/JPO-D-14-0254.1

Evans, D., Frajka-Williams, E., & Garabato, A. N. (2022). Dissipation of mesoscale eddies at a western boundary via a direct energy cascade. *Scientific Reports*, *12*(1), 1–13.

Evans, D., Frajka-Williams, E., Garabato, A. N., Polzin, K., & Forryan, A. (2020). Mesoscale eddy dissipation by a 'zoo' of submesoscale processes at a western boundary. *Journal of Geophysical Research: Oceans*, e2020JC016246.

Ferrari, R., & Wunsch, C. (2009). Ocean circulation kinetic energy: Reservoirs, sources, and sinks. *Annual Review of Fluid Mechanics*, *41*.

Gill, A. (1982). *Atmosphere-ocean dynamics (international geophysics series).* academic press.

Gill, A., Green, J., & Simmons, A. (1974). Energy partition in the large-scale ocean circulation and the production of mid-ocean eddies. *Deep sea research and oceanographic abstracts*, *21*(7), 499–528.

Gouretski, V., & Koltermann, K. (2004). WOCE global hydrographic climatology. *Berichte des BSH*, *35*, 1–52.

Gula, J., Molemaker, M., & McWilliams, J. (2015). Gulf Stream dynamics along the Southeastern U.S. Seaboard. *J. Phys. Oceanogr.*, *45*(3), 690-715.

Gula, J., Molemaker, M., & McWilliams, J. (2016). Submesoscale dynamics of a Gulf Stream frontal eddy in the South Atlantic Bight. *Journal of Physical Oceanography*, *46*(1), 305–325.

Halo, I., Penven, P., Backeberg, B., Ansorge, I., Shillington, F., & Roman, R. (2014).

Mesoscale eddy variability in the southern extension of the East Madagascar Current: Seasonal cycle, energy conversion terms, and eddy mean properties. *Journal of Geophysical Research: Oceans*, *119*(10), 7324–7356.

Harrison, D. E., & Robinson, A. R. (1978). Energy analysis of open regions of turbulent flows—Mean eddy energetics of a numerical ocean circulation experiment. *Dynamics of Atmospheres and Oceans*, *2*(2), 185–211.

Jamet, Q., Deremble, B., Wienders, N., Uchida, T., & Dewar, W. (2021). On wind-driven energetics of subtropical gyres. *Journal of Advances in Modeling Earth Systems*, *13*(4), e2020MS002329.

Kang, D., & Curchitser, E. (2015). Energetics of eddy–mean flow interactions in the Gulf Stream region. *Journal of Physical Oceanography*, *45*(4), 1103–1120.

Kelly, S. (2016). The vertical mode decomposition of surface and internal tides in the presence of a free surface and arbitrary topography. *Journal of Physical Oceanography*, *46*(12), 3777–3788.

Kelly, S., Nash, J., & Kunze, E. (2010). Internal-tide energy over topography. *Journal of Geophysical Research: Oceans*, *115*(C6).

Kelly, S., Nash, J., Martini, K., Alford, H. M., & Kunze, E. (2012). The cascade of tidal energy from low to high modes on a continental slope. *Journal of physical oceanography*, *42*(7), 1217–1232.

Li, J., Roughan, M., & Kerry, C. (n.d.). Dynamics of interannual eddy kinetic energy modulations in a western boundary current. *Geophysical Research Letters*, e2021GL094115.

Locarnini, M., Mishonov, A., Baranova, O., Boyer, T., Zweng, M., Garcia, H., ... others (2018). *World ocean atlas 2018, volume 1: Temperature* [Dataset]. ARCHIMER. Retrieved from `https://data.nodc.noaa.gov/woa/WOA18/DOC/woa18_vol1.pdf`

Lutjeharms, J. (2006). *The Agulhas Current* (Vol. 2). Springer.

Masuda, A. (1978). Group velocity and energy transport by Rossby waves. *Journal of Oceanography*, *34*(1), 1–7.

Morrow, R., Fu, L., Ardhuin, F., Benkiran, M., Chapron, B., Cosme, E., ... others (2019). Global observations of fine-scale ocean surface topography with the Surface Water and Ocean Topography (SWOT) mission. *Frontiers in Marine Science*, *6*, 232.

Müller, P., McWilliams, J., & Molemaker, M. (2005). *Routes to dissipation in the ocean: The 2D/3D turbulence conundrum.* Cambridge University Press Cambridge.

Nikurashin, M., & Ferrari, R. (2010). Radiation and dissipation of internal waves generated by geostrophic motions impinging on small-scale topography: Theory. *Journal of Physical Oceanography*, *40*(5), 1055–1074.

Paldor, N., & Lutjeharms, J. (2009). Why is the stability of the Agulhas Current geographically bi-modal? *Geophysical Research Letters*, *36*(14), n/a–n/a. Retrieved from `http://dx.doi.org/10.1029/2009GL038445` (L14604) doi: 10.1029/2009GL038445

Perfect, B., Kumar, N., & Riley, J. (2020). Energetics of Seamount Wakes. Part I: Energy Exchange. *Journal of Physical Oceanography*, *50*(5), 1365–1382.

Qiu, B., Chen, S., Klein, P., Wang, J., Torres, H., Fu, L.-L., & Menemenlis, D. (2018). Seasonality in transition scale from balanced to unbalanced motions in the world ocean. *Journal of Physical Oceanography*, *48*(3), 591–605.

Rhines, P. (1975). Waves and turbulence on a beta-plane. *Journal of Fluid Mechanics*, *69*(3), 417–443.

Scott, R., & Furnival, D. (2012). Assessment of traditional and new eigenfunction bases applied to extrapolation of surface geostrophic current time series to below the surface in an idealized primitive equation simulation. *Journal of physical oceanography*, *42*(1), 165–178.

Shchepetkin, A., & McWilliams, J. (2005). The Regional Oceanic Modeling System (ROMS): A split-explicit, free-surface, topography-following- coordinate ocean model. *Ocean Modelling*, *9*, 347-404.

Smith, K., & Vallis, G. (2001). The scales and equilibration of midocean eddies: Freely evolving flow. *Journal of Physical Oceanography*, *31*(2), 554–571.

Soufflet, Y., Marchesiello, P., Lemarié, F., Jouanno, J., Capet, X., Debreu, L., & Benshila, R. (2016). On effective resolution in ocean models. *Ocean Modelling*, *98*, 36–50.

Tedesco, P., Gula, J., Ménesguen, C., Penven, P., & Krug, M. (2019). Generation of submesoscale frontal eddies in the Agulhas Current. *Journal of Geophysical Research: Oceans*, *124*(11), 7606–7625.

Tedesco, P., Gula, J., Penven, P., & Ménesguen, C. (2022). Mesoscale Eddy Kinetic Energy budgets and transfers between vertical modes in the Agulhas Current. *Journal of Physical Oceanography*.

Torres, H., Klein, P., Menemenlis, D., Qiu, B., Su, Z., Wang, J., … Fu, L.-L. (2018). Partitioning ocean motions into balanced motions and internal gravity waves: A modeling study in anticipation of future space missions. *Journal of Geophysical Research: Oceans*, *123*(11), 8084–8105.

Venaille, A., Vallis, G., & Smith, K. (2011). Baroclinic turbulence in the ocean: Analysis with primitive equation and quasigeostrophic simulations. *Journal of Physical Oceanography*, *41*(9), 1605–1623.

Wunsch, C. (1997). The vertical partition of oceanic horizontal kinetic energy. *Journal of Physical Oceanography*, *27*(8), 1770–1794.

Wunsch, C. (2007). The past and future ocean circulation from a contemporary perspective. *Geophysical Monograph-American Geophysical Union*, *173*, 53.

Yan, X., Kang, D., Curchitser, E., & Pang, C. (2019). Energetics of eddy–mean flow interactions along the western boundary currents in the North Pacific. *Journal of Physical Oceanography*, *49*(3), 789–810.

Yang, Y., & Liang, X. S. (2016). The instabilities and multiscale energetics underlying the mean–interannual–eddy interactions in the Kuroshio Extension region. *Journal of Physical Oceanography*, *46*(5), 1477–1494.

Yang, Z., Zhai, X., Marshall, D., & Wang, G. (2021). An Idealized Model Study of Eddy Energetics in the Western Boundary "Graveyard". *Journal of Physical Oceanography*, *51*(4), 1265–1282.

Zhai, X., Johnson, H., & Marshall, D. (2010). Significant sink of ocean-eddy energy near western boundaries. *Nature Geoscience*, *3*(9), 608.

Zweng, M., Seidov, D., Boyer, T., Locarnini, M., Garcia, H., Mishonov, A., … others (2019). *World ocean atlas 2018, volume 2: Salinity* [Dataset]. ARCHIMER. Retrieved from `https://data.nodc.noaa.gov/woa/WOA18/DOC/woa18_vol2.pdf`